Perceptual error based on Bayesian cue combination drives implicit motor adaptation

Zhaoran Zhang[1, †], Huijun Wang[1, †], Tianyang Zhang[1], Zixuan Nie[1], Kunlin Wei[1,2,3,4 *]

[1]School of Psychological and Cognitive Sciences, Peking University, Beijing, China

[2]Beijing Key Laboratory of Behavior and Mental Health, Beijing, China

[3]Peking-Tsinghua Center for Life Sciences, Peking University, Beijing, China

[4]National Key Laboratory of General Artificial Intelligence, Beijing, China

[†]Zhaoran Zhang and Huijun Wang are co-first authors.

[*]Correspondence to: Kunlin Wei
School of Psychological and Cognitive Sciences
Peking University
5 Yiheyuan Road
Beijing, 100871, China
wei.kunlin@pku.edu.cn

Abstract

The sensorimotor system can recalibrate itself without our conscious awareness, a type of procedural learning whose computational mechanism remains undefined. Recent findings on implicit motor adaptation, such as over-learning from minor perturbations and swift saturation for increasing perturbation size, challenge existing theories based on sensory errors. We argue that perceptual error, arising from the optimal combination of movement-related cues, is the primary driver of implicit adaptation. Central to our theory is the linear relationship between the sensory uncertainty of visual cues and perturbation, validated through perceptual psychophysics (Experiment 1). Our theory predicts diverse features of implicit adaptation across a spectrum of perturbation conditions on trial-by-trial basis (Experiment 2) and explains proprioception changes and their relation to visual perturbation (Experiment 3). By altering visual uncertainty in perturbation, we induced unique adaptation responses (Experiment 4). Overall, our perceptual error framework outperforms existing models, suggesting that Bayesian cue integration underpins the sensorimotor system's implicit adaptation.

Introduction

To achieve and sustain effective motor performance, humans consistently recalibrate their sensorimotor systems to adapt to both internal and external environmental disturbances (Berniker & Kording, 2008; Shadmehr et al., 2010; Wolpert et al., 2011). For instance, transitioning to a high-sensitivity gaming mouse, which drives cursor movement at an accelerated rate compared to a standard computer mouse, may initially result in decreased performance in computer-related tasks. However, humans are capable of rapidly adapting to this new visuomotor mapping within a short period of time. While conscious corrections can facilitate this adaptation process, our sensorimotor system often times adapts itself implicitly without our conscious efforts (Albert et al., 2021; Krakauer et al., 2019).

While recent research has intensively examined the interplay between explicit and implicit learning systems (Albert et al., 2022; Miyamoto et al., 2020), several characteristics of implicit motor adaptation have emerged that challenge traditional theories. Conventionally, motor adaptation is conceptualized as error-based learning, in which learning accrues in proportion to the motor error experienced (Cheng & Sabes, 2006; Donchin et al., 2003; Thoroughman & Shadmehr, 2000). However, implicit adaptation exhibits an overcompensation phenomenon where the extent of adaptation surpasses the error induced by visual perturbations (Kim et al., 2018; Morehead et al., 2017). Additionally, implicit adaptation manifests a saturation effect; it increases with perturbations but plateaus across a broad range of larger perturbations (Bond & Taylor, 2015; Kim et al., 2018; Morehead et al., 2017; Neville & Cressman, 2018). These observations of overcompensation and saturation are incongruent with prevailing state-space updating

models, which presuppose that incremental learning constitutes only a fraction of the motor error (McDougle et al., 2015; Smith et al., 2006). Another aspect of implicit adaptation that remains mechanistically unexplained pertains to its impact on proprioception. In traditional motor adaptation, proprioception is biased towards the visual perturbation, maintaining a stable bias throughout the adaptation process (Ruttle et al., 2016, 2021). In contrast, implicit adaptation initially biases proprioceptive localization of the hand towards the visual perturbation, but this bias gradually drifts in the opposite direction over time (Tsay et al., 2020).

Causal inference of motor errors has been suggested to explain the discounting of large perturbations (Wei & Körding, 2009). However, the causal inference account predicts a decline in adaptation with increasing perturbation, diverging from the observed ramp-like saturation effect. (Tsay, Kim, et al., 2022) recently synthesized existing evidence to propose that implicit adaptation reaches an upper bound set by cerebellar error correction mechanisms, reflected in a ramp-like influence of vision on proprioception (Tsay, Kim, et al., 2022). While this ramp function could explain the observed saturation, the postulate of an upper bound on visual influence lacks empirical validation. Some research supports the idea of saturation in proprioceptive recalibration (Modchalingam et al., 2019), yet other studies suggest a linear increase with visual perturbations (Rossi et al., 2021; Salomonczyk et al., 2011). Additionally, current models fall short of quantitatively capturing the time-dependent shifts in proprioceptive bias associated with implicit adaptation.

In this study, we put forth a unified model that aims to account for the distinct features of implicit adaptation, based on the Bayesian combination of movement-related cues. Prior

models have overlooked the fact that visual uncertainty related to the perturbation increases with the size of the perturbation as the cursor moves further from the point of fixation and into the visual periphery (Klein & Levi, 1987; Levi et al., 1987). This is particularly pertinent for implicit adaptation that is widely investigated by the so-called error-clamp paradigm, in which participants are instructed to fixate on the target and disregard the perturbing cursor. Moreover, conventional theories of motor adaptation attribute motor error to the sensory modality of the perturbation, i.e., visual errors for visual perturbations (Tsay, Kim, et al., 2022; Wei & Körding, 2009). We propose an alternative: perceptual error drives implicit adaptation, as the perturbed sensory feedback influences the perception of the effector and, subsequently, motor adaptation. Through a series of experiments, we aim to demonstrate that combining eccentricity-induced visual uncertainty (Experiment 1) with a traditional motor adaptation model (state-space model) and a classical perception model (Bayesian cue combination) can explain both over-compensation and saturation effects (Experiment 2), as well as the time-dependent changes in proprioceptive bias (Tsay et al., 2020). Finally, to provide causal evidence supporting our Perceptual Error Adaptation (PEA) model, we manipulated visual uncertainty and observed that subsequent adaptation was attenuated for large perturbations but not for small ones—a finding that contradicts existing models but aligns well with the PEA model. Across the board, our model outperforms those based on ramp error-correction (Tsay, Kim, et al., 2022) and causal inference of errors (Wei & Körding, 2009), offering a more parsimonious explanation for the salient features of implicit adaptation.

Results

The perceptual error adaptation model with varying visual uncertainty

We start by acknowledging that the perceptual estimation of effector position is dynamically updated and influenced by sensory perturbations during motor adaptation. For implicit adaptation studied via the error-clamp paradigm, participants are required to bring their hand to the target while ignoring the direction-clamped cursor (Morehead et al., 2017). Accordingly, the perceptual estimation of the hand movement direction relies on three noisy sensory cues: the visual cue from the cursor, the proprioceptive cue from the hand, and the sensory prediction of the reaching action (Figure 1A). Without loss of generality, we posit that each cue is governed by an independent Gaussian distribution: the visual cue x_v follows $N(\theta, \sigma_v^2)$, where θ is the cursor direction and σ_v^2 is visual variance, the proprioceptive cue x_p follows $N(x_{hand}, \sigma_p^2)$, where x_{hand} is the hand movement direction and σ_p^2 is proprioceptive variance, and the sensory prediction cue x_u follows $N(T, \sigma_u^2)$, where T is the target direction and σ_u^2 is prediction variance. Participants aim for the target, expecting their hand to reach it. Using the Bayesian cue combination framework (Berniker & Kording, 2011), the perceived hand location ($\hat{x}_{Hand}$) on trial *n* can be derived:

$$\hat{x}_{Hand,n} = \sum_i W_i x_{i,n}, \ with \quad W_i = \frac{1/\sigma_i^2}{\sum_j 1/\sigma_j^2}, \ i,j = u,p,v \tag{1}$$

This estimated hand position is derived using maximum likelihood estimation from the three noisy cues. Given that the clamped cursor deviates the target by θ, the visual cue x_v biases the hand estimate $\hat{x}_{Hand}$ towards the cursor's direction. This deviation from the target direction T constitutes the perceptual error, which drives adaptation on the

subsequent trial *n+1* (Eq. 2). Consisting with existing models (Albert et al., 2022; Cheng & Sabes, 2006; Herzfeld et al., 2014; McDougle et al., 2015), trial-to-trial adaptation is modeled using a state-space equation:

$$x_{p,n+1} = Ax_{p,n} + B\left(T - \hat{x}_{Hand,n}\right), \quad (2)$$

where A is the retention rate capturing inter-movement forgetting and B is the learning rate capturing the proportion of error corrected within a trial. The interplay between forgetting and learning dictates the overall learning extent, i.e., the asymptote of x_p:

$$x_p^{asym} = -\frac{B/\sigma_v^2}{B/\sigma_p^2 + (1-A)\sum_j 1/\sigma_j^2}\theta,\ j = v, p, u \quad (3)$$

Thus, the positive influence of perturbation size θ on the adaptation extent is counterbalanced by the rise in visual uncertainty σ_v, since sensory uncertainty of various visual stimuli increases linearly with eccentricity (Klein & Levi, 1987; Levi et al., 1987). As participants are instructed to fixate on the target, an increase in θ lead to increased eccentricity. Hence, we model this linear increase in visual uncertainty by

$$\sigma_v = a + b\theta, \quad (4)$$

where *a* and *b* are free parameters. We conducted simulations of implicit adaptation with varying error clamp size (θ). The model simulation closely resembles the saturated adaptation in three independent experiments (Kim et al., 2018; Morehead et al., 2017). In fact, our PEA model predicts a concave adaptation pattern, contrasting with the ramp pattern suggested by the PReMo model (Tsay, Kim, et al., 2022). In Experiment 1, we aim to validate the assumption of a linear increase in visual uncertainty (Eq. 1); in Experiment 2, we seek to verify whether implicit adaptation adheres to a concave pattern

as prescribed by the PEA model. Subsequent experiments, namely Experiments 3 and 4, will test the model's additional novel predictions concerning changes in proprioception and the impact of experimentally manipulated visual uncertainty on adaptation, respectively.

---- insert Figure 1 here ----

Experiment 1: Visual Uncertainty Increases Linearly with Perturbation Size

To quantify visual uncertainty in a standard error-clamp adaptation setting, we employed psychometric methods. Occluded from seeing their actual hand, participants (n=18) made repetitive reaches to a target presented 10 cm straight head while an error-clamped cursor moving concurrently with one of three perturbation sizes (i.e., 4°, 16° and 64°), randomized trial-by-trial. In alignment with the error-clamp paradigm, participants were instructed to fixate on the target and to ignore the rotated cursor feedback. Eye-tracking confirmed compliance with these instructions (Figure S1). Perturbation directions were counter-balanced across trials, with equal probability of clockwise (CW) and counterclockwise (CCW) rotation. Post-movement, participants were required to judge the cursor's rotation direction (CW or CCW) relative to a briefly displayed reference point (Figure 2A & Figure 6A). Employing this two-alternative forced-choice (2AFC) task and the Parameter Estimation by Sequential Testing (PEST) procedure (Lieberman & Pentland, 1982), we derived psychometric functions for visual discrimination (Figures 6 and Figure S2). Our findings reveal a significant increase in visual uncertainty (σ_v) with

perturbation size, for both CW and CCW rotations (Friedman test, CW direction: $\chi^2(2) = 34.11$, $p = 4e\text{-}8$; CCW: $\chi^2(2) = 26.47$, $p = 2e\text{-}6$). Given the symmetry for the two directions, we collapsed data from both directions, and confirmed the linear relationship between σ_v and θ by a generalized linear model: $\sigma_v = a + b\theta$, with a = 1.853 and b = 0.309, R^2 = 0.255 ($F = 51.6$, $p = 2.53e\text{-}9$). The 95% confidence intervals (CI) for a and b are [0.440, 3.266] and [0.182, 0.435], respectively. The intercept was similar to the visual uncertainty estimated in a previous study (Tsay, Avraham, et al., 2021). The linear dependency indicates a striking seven-fold increase in visual uncertainty from a 4° perturbation to a 64° perturbation (22.641 ± 6.024° vs. 3.172 ± 0.453°).

---- insert Figure 2 here ----

Experiment 2: Visual Uncertainty Modulated Perceptual Error Accounts for Overcompensation and Saturation in Implicit Adaptation

The critical test of the PEA model lies in its ability to employ the linear function of visual uncertainty obtained from Experiment 1 to precisely explain key features of implicit adaptation. Earlier research mostly scrutinized smaller perturbation angles when reporting saturation effects (Bond & Taylor, 2015; Kim et al., 2018; Morehead et al., 2017). In contrast, Experiment 2 involved seven participant groups (n = 84) to characterize implicit adaptation across an extensive range of perturbation sizes (i.e., 2°, 4°, 8°, 16°, 32°, 64°, and 95°). After 30 baseline training cycles without perturbations, each group underwent 80 cycles of error-clamped reaching and 10 washout cycles without visual

feedback (Figure 3A). We replicated key features of implicit adaptation: it incrementally reached a plateau, and then declined during washout. Small perturbations led to overcompensation beyond visual errors (for 2°, 4°, 8°, 16° clamp sizes). Across perturbation sizes, the faster the early adaptation the larger the adaptation extent (Figure S4). Critically, the adaptation extent displayed a concave pattern: increasing steeply for smaller perturbations and tapering off for larger ones (Figure 3B). A one-way ANOVA revealed a significant group difference in adaptation extent ($F(6,83) = 12.108$, $p = 1.543e\text{-}09$). Planned contrasts indicated that 8°, 16°, and 32° perturbations did not differ from each other (all $p>0.417$, with Tukey-Kramer correction), consistent with earlier evidence of invariant implicit adaptation (Kim et al., 2018). However, 64° and 95° perturbations led to significantly reduced adaptation extents compared to 8° ($p = 3.194e\text{-}05$ and $5.509e\text{-}06$, respectively), supporting the concave pattern as a more accurate portrayal of implicit adaptation across varying perturbation size.

Importantly, the PEA model, when augmented with visual uncertainty data from Experiment 1, precisely predicts this size-dependent adaptation behavior (Figure 3B). Beyond adaptation extent, the model also accurately predicts the trial-by-trial adaptation across all seven participant groups, employing a single parameter set ($R^2 = 0.975$; Figure 3A). The model had only four free parameters ($A = 0.974$, $B = 0.208$, $\sigma_p = 11.119^o$, $\sigma_u = 5.048^o$; Table S1). Remarkably, both the retention rate A and learning rate B are consistent with previous studies focusing on visuomotor rotation adaptation (Albert et al., 2022). We also quantified proprioceptive uncertainty (σ_p) in a subset of participants (n=13) using a similar 2AFC procedure as in Experiment 1. We found that σ_p was $9.737^o \pm 5.598^o$ (Figure S6), which did not statistically differ from the σ_p value obtained from the model

fitting (two-tailed t-test, $p = 0.391$). In summary, the perceptual parameters obtained in Experiment 1, when incorporated into the PEA model, effectively explain the implicit adaptation behaviors observed in different participant groups in Experiment 2.

---- insert Figure 3 here ----

In comparative analysis, the PReMo model yields a substantially lower R^2 value of 0.749 (Figure S3B). It tends to underestimate adaptation for medium-size perturbations and overestimate it for large ones (Figure 3C; see also Figure S3B for trial-by-trial fitting). Another alternative is the causal inference model, previously shown to account for nonlinearity in motor learning (Mikulasch et al., 2022; Wei & Körding, 2009). Although this model has been suggested for implicit adaptation (Tsay, Avraham, et al., 2021), it fails to reproduce the observed concave adaptation pattern (Figures S3C and 3D). The model aligns well with adaptations to medium-size perturbations (8°, 16°, and 32°) but falls short for small and large ones, yielding an R^2 value of 0.711 (see Figure S3C for trial-by-trial fits). Model comparison metrics strongly favor the PEA model over both the PReMo and causal inference models, as evidenced by AIC scores of 2255, 3543, and 3283 for the PEA, PReMo, and causal inference models, respectively (Table S2). In summary, it is the eccentricity-induced visual uncertainty that most accurately accounts for the implicit adaptation profile across a broad spectrum of perturbation sizes, rather than saturated visual influence or causal inference of error.

240 *Experiment 3: Cue Combination Accounts for Changes in Proprioception During Implicit*
241 *Adaptation*

242 Motor adaptation not only recalibrates the motor system but also alters proprioception
243 (Rossi et al., 2021) and even vision (Simani et al., 2007). In traditional motor adaptation
244 involving both explicit and implicit components, the perceived hand location is initially
245 biased towards the visual perturbation and subsequently stabilizes (Ruttle et al., 2016).
246 However, in implicit adaptation, the perceived hand location initially aligns with but later
247 drifts away from the visual feedback (Tsay et al., 2020). The PReMo model proposes that
248 this drift comprises two phases: initial proprioceptive recalibration and subsequent visual
249 recalibration (Tsay, Kim, et al., 2022), however, this assumption is lack of empirical
250 validation. In contrast, we suggest that the perceived hand location is based on the same
251 Bayesian cue combination principle. In this framework, the perceived hand location at the
252 end of each reach is influenced by both the proprioceptive cue (x_p) and the estimated
253 hand position under the influence of clamped feedback ($\hat{x}_{Hand}$, Eq. 1).

254 During early adaptation, $\hat{x}_{Hand}$ is biased towards the clamped feedback, while x_p remains
255 near the target as the motor system has yet to adapt (Figure 4A). This results in an initial
256 negative proprioceptive bias. As adaptation progresses, although $\hat{x}_{Hand}$ remains biased,
257 x_p gradually shifts in the positive direction due to adaptation, resulting in an increasingly
258 positive proprioceptive bias. Remarkably, the PEA model can predict these temporal
259 changes in proprioception with high accuracy (R^2 = 0.982; Figure 4A).

260 If the hand estimate $\hat{x}_{Hand}$ indeed influences proprioceptive recalibration during
261 adaptation, our PEA model can make specific quantitative predictions about the
262 relationship between proprioception changes and visual perturbation size. While

traditional visuomotor paradigms suggest either invariant (Modchalingam et al., 2019) or linear increases in proprioceptive recalibration with visual-proprioceptive discrepancy (Salomonczyk et al., 2011), the PEA model prescribes a concave function in relation to visual perturbation size (Figure 4B).

To empirically test this prediction, Experiment 3 (n=11) measured participants' proprioceptive recalibration during implicit adaptation, using a procedure similar to the error-clamp perturbations in Experiment 2. After each block of six adaptation trials, participants' right hands were passively moved by a robotic manipulandum, and they indicated the perceived direction of their right hand using a visually represented "dial" controlled by their left hand (Figure 7B). This method quantifies proprioceptive recalibration during adaptation (Cressman & Henriques, 2009). Each adaptation block was followed by three such proprioception test trials. The alternating design between adaptation and proprioception test blocks allowed us to assess proprioceptive biases across varying perturbation sizes, which consisted of ±10°, ±20°, ±40°, and ±80°, to covering a wide range (Figure 4D).

Our findings confirmed a typical proprioceptive recalibration effect, as the perceived hand direction was biased towards the visual perturbation (Figure 4E). Importantly, the bias in the initial proprioception test trial exhibited a concave function of perturbation size. A one-way repeated-measures ANOVA revealed a significant effect of perturbation size ($F(3,30)=3.603, p=0.036$), with the 20° and 40° conditions displaying significantly greater proprioceptive bias compared to the 80° condition (pairwise comparisons: 20° v.s. 80°, $p = 0.034$; 40° v.s. 80°, $p = 0.003$). The bias was significantly negative for 20° and 40° conditions ($p = 0.005$ and $p = 0.007$, respectively with one-tailed t-test), but not for 10°

and 80° condition (p = 0.083 and p = 0.742, respectively). This concave pattern aligns well with the PEA model's predictions (Figure 4B), further consolidating its explanatory power.

---- insert Figure 4 here ----

This stands in contrast to the PReMo model, which assumes a saturation for the influence of the visual cue on the hand estimate (Eq. 12-13). As a result, PReMo's predicted proprioceptive bias follows a ramp function, deviating substantially from our empirical findings (Figure 4C). The causal inference model, which mainly focuses on the role of visual feedback in error correction, lacks the capability to directly predict changes in proprioceptive recalibration.

Interestingly, we observed that the proprioceptive bias reduced to insignificance by the third trial in each proprioception test block (one-tailed t-test, all $p > 0.18$; Figure 4E, yellow line). This suggests that the influence from implicit adaptation – manifested here as trial-by-trial updates of the perceived hand estimate $\hat{x}_{Hand}$ – decays rapidly over time.

Experiment 4: Differential Impact of Upregulated Visual Uncertainty on Implicit Adaptation Across Perturbation Sizes

Thus far, we have presented both empirical and computational evidence underscoring the pivotal role of perceptual error and visual uncertainty in implicit adaptation. It is crucial to note, however, that this evidence is arguably correlational, arising from natural

variations in visual uncertainty as a function of perturbation size. To transition from correlation to causation, Experiment 4 (n = 19) sought to directly manipulate visual uncertainty by blurring the cursor, thereby offering causal support for the role of multimodal perceptual error in implicit adaptation.

By increasing visual uncertainty via cursor blurring, we hypothesized a corresponding decrease in adaptation across all perturbation sizes. Notably, the PEA model predicts a size-dependent attenuation in adaptation: the reduction is less marked for smaller perturbations and more pronounced for larger ones (Figure 5A). This prediction diverges significantly from those of competing models. The PReMo model, operating under the assumption of a saturation effect for large visual perturbations, predicts that cursor blurring will only influence adaptation to smaller perturbations, leaving adaptation to larger perturbations unaffected (Figure 5B). The causal inference model makes an even more nuanced prediction: it anticipates that the blurring will lead to a substantial reduction in adaptation for small perturbations, a diminishing effect for medium perturbations, and a potential reversal for large perturbations (Figure 5C). This prediction results from the model's core concept that causal attribution of the cursor to self-action—which directly dictates the magnitude of adaptation—decreases for small perturbations but increases for large ones when overall visual uncertainty is elevated.

---- insert Figure 5 here ----

Starting from the above predictions, Experiment 4 was designed to assess the impact of elevated visual uncertainty across small (4°), medium (16°), and large (64°) perturbation sizes. Visual uncertainty was augmented by superimposing a Gaussian blurring mask on the cursor (Burge et al., 2008). Each participant performed reaching tasks with either a standard or blurred clamped cursor for a single trial, bracketed by two null trials devoid of cursor feedback (Figure 5D). These three-trial mini-blocks permitted the quantification of one-trial learning as the directional difference of movements between the two null trials. To preclude the cumulative effect of adaptation, perturbation sizes and directions were randomized across mini-blocks.

Crucially, our findings corroborated the predictions of the PEA model: visual uncertainty significantly diminished adaptation for medium and large perturbations (16° and 64°), while leaving adaptation for small perturbations (4°) largely unaffected (Figure 5E). A two-way repeated-measures ANOVA, with two levels of uncertainty and three levels of perturbation size, revealed a significant main effect of increased visual uncertainty in reducing implicit adaptation ($F(1,18) = 42.255$, $p = 4.112e\text{-}06$). Furthermore, this effect interacted with perturbation size ($F(2,36) = 5.391$, $p = 0.012$). Post-hoc analyses demonstrated that elevated visual uncertainty significantly attenuated adaptation for large perturbations ($p = 2.877e\text{-}04$, $d = 0.804$ for 16°; $p = 1.810e\text{-}05$, $d = 1.442$ for 64°) but exerted no such effect on small perturbations ($p = 0.108$, $d = 0.500$). These empirical outcomes are not congruent with the predictions of either the PReMo or the causal inference models (Figure 5B and 5C). This lends compelling empirical support to the primacy of perceptual error in driving implicit adaptation, as posited by our PEA model.

Discussion

In this study, we elucidate the central role of perceptual error, derived from multimodal sensorimotor cue integration, in governing implicit motor adaptation. Utilizing the classical error-clamp paradigm, we uncover that the overcompensation observed in response to small perturbations arises from a sustained perceptual error related to hand localization, and the saturation effect commonly reported in implicit adaptation is not an intrinsic characteristic but is attributable to increasing sensory uncertainty with increasing visual perturbation eccentricity—a factor hitherto neglected in existing models of sensorimotor adaptation. Contrary to conventional theories that describe implicit adaptation as either saturated or invariant (Kim et al., 2018; Tsay, Kim, et al., 2022), our data reveal a concave dependency of implicit adaptation on visual perturbation size, characterized by diminishing adaptation in response to larger perturbations. Notably, our Perceptual Error Adaptation (PEA) model, calibrated using perceptual parameters from one set of participants, provides a robust account of implicit adaptation in separate groups subjected to varying perturbations. The model further successfully captures the perceptual consequences of implicit adaptation, such as the continuous shifts in proprioceptive localization during the adaptation process (Tsay et al., 2020) and its correlation with perturbation size. Lastly, we manipulated visual uncertainty independently of perturbation size and demonstrated that this selectively attenuated adaptation in the context of larger perturbations while leaving smaller perturbations unaffected. These empirical results, inconsistent with predictions from existing models, underscore the conceptual and quantitative superiority of our PEA model. In summary, our findings advocate for a revised

375 understanding of implicit motor adaptation, suggesting that it is governed by Bayesian
376 cue combination-based perceptual estimation of effector localization.

377 Bayesian cue combination has been established as a foundational principle in various
378 perceptual phenomena, both intra- and inter-modally (Seilheimer et al., 2014). It has also
379 been implicated in motor adaptation (Burge et al., 2008; He et al., 2016; Körding &
380 Wolpert, 2004; Wei & Körding, 2010). However, previous studies have largely focused on
381 experimentally manipulating sensory cue uncertainty to observe its effects on adaptation
382 (Burge et al., 2008; Wei & Körding, 2010), similar to our Experiment 4. What has been
383 largely overlooked is the natural covariance between visual uncertainty and perturbation
384 size, which, when incorporated into classical state-space models, provides a compelling
385 explanation for implicit adaptation.

386 The causal inference framework (Wei & Körding, 2009) fails to adequately predict
387 sensorimotor changes in implicit adaptation. For instance, it underestimates the
388 adaptation extent for large perturbations and incorrectly predicts that increasing visual
389 uncertainty would augment, rather than reduce, adaptation to large perturbations. We
390 postulate that causal inference is more relevant to motor learning dominated by explicit
391 processes, such as traditional visuomotor rotations, rather than in implicit adaptations
392 where cue combination is obligatory.

393 Similar to our PEA model, the PReMo model also incorporates the integration of multiple
394 sensory cues. But two models differ fundamentally in their conceptualization of how these
395 cues contribute to the error signal. The PReMo model posits two intermediate perceptual
396 variables with Bayesian cue integration: a visual estimate of the cursor and a
397 proprioceptive estimate of the hand (Tsay, Kim, et al., 2022). The final error signal in

PReMo is presumed to be a proprioceptive error, not from further Bayesian cue combination, but from a visual-to-proprioceptive bias that is governed by a predetermined, ramp-like visual influence that saturates around a 6–7° visual-proprioceptive discrepancy (Eq. 13). These assumptions lack empirical validation. Our findings in Experiment 3 indicate that proprioceptive recalibration follows a concave function with respect to visual perturbation size, contradicting the ramp-like function assumed by PReMo. Moreover, the presupposed ramp-like visual influence generates a rigid prediction for a ramp-like adaptation extent profile, which is at odds with the concave adaptation pattern we observed in Experiment 2 and in a similar study involving trial-by-trial learning (Tsay, Avraham, et al., 2021). Furthermore, PReMo predicts that increasing visual uncertainty will selectively reduce adaptation to small perturbations while sparing large ones. This is inconsistent with our findings in Experiment 4, which demonstrated that increased visual uncertainty substantially impacted adaptation more to larger perturbations than to small ones. Lastly, PReMo's reliance on a proprioceptive bias constrains its ability to account for the temporal shifts in perceived hand location during adaptation (Tsay et al., 2020). In contrast to PEA's unified approach, PReMo must resort to separate mechanisms of proprioceptive and visual recalibration at different phases of adaptation to explain these shifts. In summary, the PReMo model's assumptions introduce limitations that make it less consistent with empirical observations, particularly concerning the nonlinearities observed in both motoric and perceptual aspects of implicit adaptation.

Our research contributes to an ongoing debate concerning the driving forces behind error-based motor learning, specifically addressing the question of whether implicit adaptation is driven by target error or sensory prediction error (Albert et al., 2022; Izawa & Shadmehr,

2011; Leow et al., 2020; Mazzoni & Krakauer, 2006; McDougle et al., 2015; Miyamoto et al., 2020; Taylor & Ivry, 2011; Tseng et al., 2007). Most empirical data fueling this debate stem from traditional motor adaptation paradigms where explicit and implicit learning co-occur and interact. In these paradigms—visuomotor rotation being a prime example—target error is defined as the disparity between the target and the perturbed cursor, while sensory prediction error is the disparity between the predicted and actual cursor. Both types of error are sensory (specifically, visual) in nature, yet they differ due to the misalignment between the predicted or desired cursor direction and the target direction, which is induced by explicit learning (Taylor et al., 2014).

By employing the error-clamp paradigm, our study was able to isolate implicit learning, thereby eliminating potential confounds from explicit learning. Interestingly, in this paradigm, the target error and sensory prediction error effectively refer to the same visual discrepancy, as both the predicted and target directions are aligned. Despite this, classical state-space models, which utilize this visual error, fail to account for the nuanced features of implicit adaptation (Tsay, Kim, et al., 2022). In contrast, our PEA model reframes the perturbing cursor as a visual cue influencing the perceptual estimation of hand location, rather than as a source of visual error. The resultant bias in hand estimation from the desired target serves as the actual error signal. This leads us to posit that the error signal driving implicit sensorimotor adaptation is fundamentally perceptual, rather than sensory. From a normative standpoint, this perceptual error could be construed either as a predictive or performance error (Albert et al., 2022), but importantly, it is not tied to a specific modality (i.e., vision or proprioception). Instead, it directly pertains to the perceptual estimate that is crucial for task execution, i.e., bringing the hand to the target.

The concept of perceptual error-driven learning can be extrapolated to various motor adaptation paradigms, including those involving explicit learning. For instance, in visuomotor rotation tasks, explicit learning manifests as a deviation in the aiming direction from the visual target, whereas implicit learning manifests as a further deviation the actual hand position from this aiming direction (Taylor et al., 2014). Even in the presence of explicit learning, the perturbed cursor continues to bias the perceptual estimate of the hand, thereby potentially driving implicit adaptation. In this scenario, the perceptual error is defined as the difference between the perceptual estimate of the hand and the altered aiming direction, which serves as the new "target" when explicit learning is in play. Our PEA model would predict similar saturation effects in implicit adaptation for this conventional adaptation paradigm, similar to for the error-clamp paradigm. Indeed, evidence from the conventional adaptation paradigm suggests that its implicit adaptation follows either a saturation effect (Bond & Taylor, 2015; Neville & Cressman, 2018) or a concave pattern (Tsay, Haith, et al., 2022) across a range of perturbation sizes. Furthermore, according to the PEA framework, this perceptual error is anchored on the aiming target, thereby naturally predicting that implicit and explicit adaptations should interact in a complementary manner, a notion that aligns with recent theories on their interaction (Albert et al., 2022; Miyamoto et al., 2020). Future research is warranted to further investigate the role of perceptual error in driving implicit learning across diverse motor learning paradigms.

Our study provides a new angle on explaining proprioceptive changes during motor adaptation, advocating for a Bayesian cue combination framework. Previously, the change in proprioceptive hand localization during motor adaptation has been ascribed to

visual-proprioceptive discrepancy-induced recalibration (Ruttle et al., 2018; Salomonczyk et al., 2013) and/or altered sensory prediction driven by the adapted forward internal model (Mostafa et al., 2019; 't Hart & Henriques, 2016). To dissect these components, researchers have often compared proprioceptive localization in actively moved (Tsay et al., 2020) versus passively placed (passive localization, e.g., Experiment 3) hands during adaptation, attributing the smaller bias in passive localization to recalibration alone. The difference between the two is then considered to reflect altered sensory prediction due to motor adaptation (Mostafa et al., 2019; Rossi et al., 2021). But these conceptual divisions lack computational models for validation. For instance, researchers have proposed that proprioceptive recalibration in visuomotor adaptation is either a fixed proportion (e.g., 20%) of the visual-proprioceptive discrepancy (Henriques & Cressman, 2012; Ruttle et al., 2021) or largely invariant (Modchalingam et al., 2019). In fact, cross-sensory calibration typically follows the Bayesian principle, as shown in other task paradigms other than motor adaptation (Stetson et al., 2006; Wozny & Shams, 2011). Our Experiment 3 shows that proprioceptive recalibration exhibits a concave, instead of invariant or proportional, dependency to visual perturbation size, a finding follows the Bayesian principles of cue combination. Our results also confirm that the critical cue for passive localization is the biased perceived hand position ($\hat{x}_{Hand}$) fueled by adaptation.

The same Bayesian framework applies to active localization, though this time $\hat{x}_{Hand}$ is to be combined with the proprioceptive cue from the adapted hand. In this sense, active localization indeed serves as a multifaceted reflection of both the internal model and proprioceptive recalibration (Mostafa et al., 2019; Rossi et al., 2021). Specifically, the proprioceptive cue continuously drifts by the adapted internal model, while the perceived

hand position encapsulates the effects of proprioceptive recalibration. During the initial stages of perturbation, the immediate negative bias in active localization is predominantly attributable to rapid proprioceptive recalibration. This is evidenced by a sudden shift in the estimated hand position ($\hat{x}_{Hand}$; Figure 4A), occurring before the internal model has had sufficient time to adapt.

Then, why does active localization in traditional motor adaptation paradigms yield a largely stable bias (Ruttle et al., 2016, 2021)? We postulate that the rapid explicit learning leads to a quick asymptotic adaptation, while previous investigations have predominantly measured active localization after adaptation has plateaued (Henriques & Cressman, 2012; Modchalingam et al., 2019; Mostafa et al., 2019; Salomonczyk et al., 2011, 2013; Tsay, Kim, et al., 2021). Consequently, these studies may overlook the evolving effect of the adaptation. In contrast, the gradual nature of implicit adaptation provides a unique opportunity to uncover the underlying mechanisms governing changes in proprioception during the adaptation process.

Notably, our model aligns with previous findings that show a positive correlation between proprioceptive recalibration and motor adaptation based on individual differences (Ruttle et al., 2021; Salomonczyk et al., 2013; Tsay, Kim, et al., 2021). Unlike existing theories that posit proprioceptive recalibration either as a component of (Modchalingam et al., 2019; Mostafa et al., 2019; Ruttle et al., 2021) or a driver for implicit adaptation (Tsay, Kim, et al., 2022), our PEA model provides a mechanistic and empirically testable framework. It posits that the misestimation of hand position ($\hat{x}_{Hand}$) —induced by the recent perturbation—serves as the driving factor for both implicit adaptation and changes in proprioception. This misestimation is perturbation-dependent, resulting in both implicit

adaptation and proprioceptive recalibration exhibiting a concave profile relative to perturbation size. Updated on a trial-by-trial basis, this misestimation exerts immediate effects, manifesting as an abrupt negative bias (Figure 4A). Additionally, its influence decays rapidly, becoming negligible within three trials (Figure 6C). These converging lines of evidence strongly suggest that perceptual misestimation of hand position is central to the process of proprioceptive recalibration during adaptation.

Our findings contribute nuanced perspectives to the modulation of implicit learning rate by factors beyond visual perturbation size. Previous studies have shown that environmental inconsistency -- defined as the inconsistency of visual errors -- reduced the rate (Herzfeld et al., 2014; Hutter & Taylor, 2018) or asymptote (Albert et al., 2021) of implicit adaptation. Baseline motor variance in unperturbed conditions has been shown to increase implicit adaptation rate, proposed as a sign of better exploratory learning (Wu et al., 2014). These studies interpret such phenomena as parametric changes in the learning rate in relation to visual errors, conceptualized as alterations to the *B* parameter in existing models. However, apparent change in learning rate to visual errors does not necessarily signify parametric modification, but may attribute to other factors that influence the use of visual cues (He et al., 2016), such as visual uncertainty in our case. Previous research has also pointed to alternative factors like error discounting based on causal inference of error (Wei & Körding, 2009), proprioceptive uncertainty (Ruttle et al., 2021; Tsay, Kim, et al., 2021), and state estimation uncertainty (He et al., 2016; Wei & Körding, 2010). Our work suggests a shift in perspective: the driving error signal for implicit learning should be considered as perceptual, rather than merely visual. This

paradigmatic shift could serve as a cornerstone for future research aimed at understanding how learning rates adapt under varying conditions.

Our new framework opens avenues for exploring the memory characteristics of implicit learning. Traditional motor adaptation often exhibits 'savings,' or accelerated relearning upon re-exposure to a perturbation (Della-Maggiore & McIntosh, 2005; Huberdeau et al., 2019; Krakauer et al., 2005; Landi et al., 2011). In contrast, implicit adaptation has been found to exhibit a decreased learning rate during re-adaptation (Avraham et al., 2021), a phenomenon attributed to conditioning (Avraham et al., 2021) or associative learning mechanisms (Avraham et al., 2022). Investigating this 'anti-saving' effect will yield insights into the unique memory properties of implicit learning. Although our current PEA model is structured around single-epoch learning and does not directly address this question, it does raise new, testable hypotheses. For example, is the reduced adaptation rate during relearning attributable to a down-weighting of perturbed visual feedback in cue combination, or does it reflect a parametric alteration in the learning rate? Another noteworthy aspect of implicit learning is its remarkably slow decay rate. It has been observed that the number of trials required to washout the implicit adaptation exceeds the number of trials needed to establish it (Avraham et al., 2021; Tsay et al., 2020). In the context of our perceptual error framework, this raises the possibility that washout phases might be governed by state updating involving a distinct set of sensorimotor cues or an alternative updating mechanism, such as memory formation and selection (Oh & Schweighofer, 2019).

Methods

Participants

We recruited 115 college students from Peking University (77 females, 38 males, 22.05 ± 2.82 years, mean ± SD). Participants were all right-handed according to the Edinburgh handedness inventory (Oldfield, 1971) and had normal or corrected-to-normal vision. Participants were naïve to the purpose of the experiment and provided written informed consent, which was approved by the Institutional Review Board of the School of Psychological and Cognitive Sciences, Peking University. Participants received monetary compensation upon completion of the experiment.

Apparatus

In Experiment 1, 2 and 4, participants were seated in front of a vertically-placed LCD screen (29.6 x 52.7 cm, Dell, Round Rock, TX, US). They performed the movement task with their right hand, holding a stylus and slide it on a horizontally placed digitizing tablet (48.8 x 30.5 cm, Intuos 4 PTK-1240, Wacom, Saitama, Japan). In Experiment 1, a keyboard was provided to the participants' left hand to enable them to report the direction of visual stimuli in the discrimination task. A customized wooden shelter was placed above the tablet to block the peripheral vision of the right arm. In Experiment 1 and 4, participants placed their chin on a chin rest attached on the wooden shelter to stabilize their head. Their eye movement was recorded by an eye tracker (Tobii pro nano, Tobii, Danderyd Municipality, Sweden) affixed at the lower edge of the screen. The sampling rate was 160-200 Hz for the tablet and 60 Hz for the eye tracker.

Experiment 3 was conducted using the KINARM planar robotic manipulandum with a virtual-reality system (BKIN Technologies Ltd., Kingston, Canada). Participants seated in a chair and held the robot handles with their left and right hands (Figure 7). The movement task was performed with the right handle and the left handle was used to indicate the perceived direction of right hand in the proprioception test. A semi-silvered mirror was placed below the eye level to block the vision of the hands and the robotic manipulandum; it also served as a display monitor.

Experiment 1: measuring visual uncertainty in error-clamp adaptation

Eighteen among twenty participants finished the reaching with clamped error feedback and visual discrimination task in 3 consecutive days, two participants withdrew during the experiment. Participants made reaching movement by sliding the stylus from a start position at the center of the workspace to towards a target (Figure 6A). The start position, the target, and the cursor were represented by a gray dot, a blue cross and a white dot on the screen, respectively. All these elements had a diameter of 5mm. The procedure of the motor and visual discrimination task is illustrated in Figure 2A. To initiate a trial, participates moved the cursor into the start position. Following an 800ms holding period, a target appeared 10 cm away in twelve o'clock direction and participants were instructed to slide through the target rapidly while maintaining a straight hand trajectory. The trial terminated when the distance between the hand and the start position exceeded 10 cm, regardless of whether the target was hit. A warning message, "too slow", would appear on the screen if participants failed to complete the trial within 300 ms after initiating the movement. Each practice day began with 60 standard reaching trials, during which veridical feedback about hand location was provided by the cursor. The target would

change from blue to green if the cursor successfully passed through it. In subsequent visual clamp trials, the cursor moved along a predetermined direction set by the perturbation angle, while its position was updated in real-time based on the hand's location. The cursor's distance from the start position was equal to the distance between the hand and the start position until the end of the trial.

Following each trial, the cursor remained frozen at its final position for an additional 800 ms before disappearing. The visual discrimination task commenced 1000 ms thereafter. A yellow reference point, located 10 cm from the start position, was displayed for 150 ms near the cursor's final position (Figure 2A & Figure 6A). Subsequently, all visual stimuli, except for the blue cross at the start position, were removed from the screen. Participants were then required to judge whether the reference point was situated in a clockwise (CW) or counterclockwise (CCW) direction relative to the cursor's final position and to report their judgment by pressing a key on the keyboard. Participants were informed that they no longer controlled the direction of cursor movement during the task. They were instructed to fixate their gaze on either the start position or the blue cross during the motor task, while actively ignoring the white cursor. During the discrimination task, they were required to maintain their gaze on the blue cross. Eye movements were monitored in real-time using an eye tracker. Participants received a warning if their gaze was detected outside a 75-pixel-wide band-shaped region centered on the line of gaze four consecutive times during the experiment (Figure S1).

---- insert Figure 6 here ----

In each trial, the angular deviation between the error-clamped cursor and the reference point was determined using a PEST procedure (Lieberman & Pentland, 1982). Figure 6C-D illustrates the evolution of the deviation angle and step size for an exemplary participant experiencing a -16° perturbation. In each round, the deviation commenced at 30° (indicated by yellow points in Figure 6C-D) and was altered by one step size following each trial. The initial step size was set at 10° and was halved whenever the direction judgment changed (i.e., from "CW" to "CCW" or vice versa). For a specific perturbation angle, the initial deviation always started from the CW direction for the first round and flipped the direction at the beginning of the next round. A round terminated either when the step size fell below a predefined criterion (indicated by the red line in Figure 6D) or when the trial count exceeded 30. Six perturbation angles were randomly interleaved (Figure 6B), and the experiment concluded when four complete rounds of the PEST procedure had been completed for each perturbation angle. Consequently, the total number of trials varied among participants and across practice days. Additionally, for some perturbation angles, more than four complete rounds could be conducted in a single day.

Experiment 2: Motor adaptation with different perturbation size

Eighty-four participants were randomly allocated into seven groups, each comprising 12 individuals. Each group performed a motor adaptation task featuring clamped visual feedback at different perturbation angles: 2°, 4°, 8°, 16°, 32°, 64°, and 95°. As in Experiment 1, participants were instructed to slide rapidly and directly through the target, which was represented by a blue dot rather than a cross. In each trial, the target appeared at one of four possible locations (45°, 135°, 225° or 315° counter-clockwise from the

positive x-axis). The sequence of target locations was randomized, yet constrained so that all four positions appeared in cycles of four trials. Each group commenced with a baseline session that included 15 cycles of reaching trials with veridical feedback, followed by 15 cycles without visual feedback. Subsequently, during the perturbation session, participants completed 80 cycles of training trials featuring the error-clamped cursor with one perturbation angle (i.e., clamp size), depending on their group assignment. To assess the aftereffect, a session comprising 10 cycles of movement without visual feedback was administered.

Experiment 3: Proprioception test with different perturbation sizes

Eleven participants were recruited for testing their proprioception recalibration. This experiment incorporated two types of trials: reaching trials and proprioception test trials. During the reaching trials, participants were instructed to aim for a target, which could appear at one of three possible locations (25°, 45°, or 65° counter-clockwise from the positive x-axis, as represented by light blue dots in Figure 4C, right panel). The task was similar to those in Experiments 1 and 2, with the key difference being that participants performed the task using KINARM robots (as depicted in Figure 7A). The dimensions and relative distances of the visual stimuli remained consistent with those used in Experiments 1 and 2. As in previous experiments, three kinds of visual feedback were provided during different sessions: no visual feedback, veridical feedback, and feedback featuring an error-clamped cursor.

In the proprioception test, participants were instructed to hold the robot's right handle and wait for passive movement by the robot to one of six proprioception targets (small red dots in Figure 4C, right panel). These targets were spaced at 10° intervals, ranging from

20° to 70° counter-clockwise from the positive x-axis, and flanked the three reaching targets. The passive movement lasted for 1,000 ms and followed a straight-line path at a speed consistent with a minimum jerk velocity profile. During this movement, a ring with a 10 cm radius, centered at the start position, was displayed on the screen (depicted as a red arc in Figure 7B). The cursor was also replaced by a ring, its radius expanding as the hand moved toward the proprioception target.

After the right hand reached the proprioception target, participants were instructed to maintain their right hand's position. Using the left handle, they were then asked to indicate the perceived location of their right hand. The position of the left handle was mapped to the rotation of a "dial," which was constrained to the target arc.

---- insert Figure 7 here ----

The position of $\boldsymbol{h}_p$ was displayed on the target arc as a small red rectangle (a visual "dial," as shown in Figure 7B). Participants were instructed to indicate the location of their right hand by moving the red rectangle to the position they perceived as accurate. The final position of $\boldsymbol{h}_p$ was recorded when its angular velocity remained below 1 degree/second for a duration exceeding 1000 ms. The proprioceptive bias was then calculated as the angular deviation between the actual hand position ($\boldsymbol{h}_R$) and the perceived hand position ($\boldsymbol{h}_p$).

Reaching trials and proprioception test trials were organized into blocks (Figure 4D). Each reaching block consisted of 6 trials, targeting 3 different locations with 2 repetitions each.

Each reaching block was followed by a proprioception test block consisting of 3 trials. In these test trials, the robot moved the participant's right hand toward a target position near one of the three reaching targets. These test targets were randomly chosen from six possible locations (Figure 4C, right panel). The entire experiment comprised 40 reaching blocks and 40 subsequent proprioception test blocks. The first four reaching blocks provided veridical cursor feedback, the next four offered no cursor feedback, and the remaining 32 featured one of eight possible perturbation sizes (±10°, ±20°, ±40°, and ±80°). The size of the perturbation was randomized between blocks.

Experiment 4: upregulating visual uncertainty affects implicit adaptation

Nineteen participants from Experiment 1 completed Experiment 4. The reaching task employed the same setup as in Experiment 1. However, instead of performing perceptual judgments of cursor motion direction, participants engaged in movements with one of three types of cursor feedback: veridical feedback, no feedback, and feedback with clamped perturbation. To assess the influence of visual uncertainty on implicit learning, we modified the cursor to appear blurred in half of the clamped trials. The blurring mask had a diameter of 6.8 mm, and the color intensity decreased from the cursor's center following a two-dimensional Gaussian distribution with $\sigma_x = \sigma_y = 1.4$ mm. As depicted in Figure 5D, participants underwent the same procedures across three consecutive days. Each day consisted of 60 baseline trials, followed by 15 training blocks designed to assess single-trial learning. Within each training block, 12 trials featured an error-clamped cursor, each flanked by a trial without feedback. The difference between two adjacent no-feedback trials served as a measure of single-trial learning at specific perturbation sizes. Each of the 12 perturbation trials was randomly assigned one of 12 possible perturbations,

comprising two cursor presentations (blurred or clear) and six clamp sizes (±4°, ±16°, ±64°).

Data analysis

Processing of kinematic data

In Experiments 1, 2, and 4, hand kinematic data were collected online at a sampling rate ranging between 160 and 200 Hz and subsequently resampled offline to 125 Hz. The movement direction of the hand was determined by the vector connecting the start position to the hand position at the point where it crossed 50% of the target distance, i.e., 5 cm from the start position.

In Experiment 3, hand positions and velocities were directly acquired from the KINARM robot at a fixed sampling rate of 1 kHz. The raw kinematic data were smoothed using a fifth-order Savitzky-Golay filter with a window length of 50 ms. Owing to the high temporal resolution and reliable velocity profiles provided by the KINARM system, the heading direction in Experiment 3 was calculated as the vector connecting the start position to the hand position at the point of peak velocity.

Psychometric curve

For the visual discrimination task, data of all three days were pooled together, the probability of responding that "the reference point was in the counter-clockwise direction of the cursor" was calculate as *p* for all angle differences (Figure S2). At each perturbation size, a logistic function was used to fit the probability distribution for individual participants:

$$p = 1/(1 + e^{-k(x-x_0)}), \quad (5)$$

where k is the slope and x_0 is the origin of the logistic function. The visual uncertainty was defined as the angle differences between 25% and 75% of the logistic function:

$$\sigma_v = \frac{\log(p_2/(1-p_2)) - \log(p_1/(1-p_1))}{k}, \quad (6)$$

where $p_1 = 25\%$ and $p_2 = 75\%$.

Statistical analysis

In Experiment 1, since the visual uncertainty σ_v follows a non-negative skewed distribution among participants, it violated the assumption of the ANOVA test. We thus applied Friedman's nonparametric test to determine whether σ_v changes with the perturbation angle θ. Specifically, σ_v for both positive and negative θ were subjected to Friedman's test separately, with θ serving as the factor. Given the symmetry between positive and negative θ, we pool the data to quantify the linear dependency of σ_v on the absolute θ (Eq. 4). Because σ_v is expected to be always positive, we assume that it is generated from a gamma distribution rather than a normal distribution. Thus, the data was fitted by a generalized linear regression model with the absolute value of θ as independent variable and σ_v as dependent variable.

In Experiment 2, the adaptation extent was defined as the mean hand angles in the last 10 cycles in the perturbation phase (cycle 101-110). A one-way ANOVA with perturbation size serving as the factor to examine its influence on the adaptation extent. Pairwise post-hoc comparisons were conducted using Tukey-Kramer correction.

In Experiment 3, proprioceptive recalibration was quantified as the angular difference between the perceived and actual hand directions. A one-way repeated-measures ANOVA was conducted on the data of first trial, using perturbation size as the within-

subject factor. Greenhouse-Geisser corrections were applied when the assumption of sphericity was violated (Kirk, 1968). Multiple pairwise comparisons were conducted among different perturbation sizes for the first proprioception test. To determine if the proprioceptive biases were significantly different from zero, one-tailed (left) *t*-tests were conducted separately for the first and third proprioception test trials at each perturbation size.

In Experiment 4, the single-trial learning data was subjected to a 2 (visual uncertainty) x 3 (perturbation size) repeated-measures ANOVA. Greenhouse-Geisser corrections were applied as above, and the simple main effect of visual uncertainty was tested for each of the three perturbation sizes.

Model fitting and simulations

Perceptual Error Adaptation (PEA) model

Model fitting for adaptation extent as a function of perturbation size. To fit the adaptation extent data from three different experiments in previous studies in (Kim et al., 2018; Morehead et al., 2017), Eq. 3 and Eq. 4 were modified for simplification. To avoid overfitting of the small dataset, we reduced the number of model parameters by assuming that $\hat{x}_{Hand}$ asymptote to the target direction in the final adaptation trials that are used for computing adaptation extent, thus the retention rate $A \equiv 1$. Insert Eq. 4 to Eq. 3, the asymptote hand angle with different perturbation size is:

$$x_p^{asym} = -\left(\frac{\sigma_p/a}{1+(b/a)\theta}\right)^2\theta. \quad (7)$$

Two ratio parameters $R_{1,ext} = \sigma_p/a$ and $R_{2,ext} = b/a$ were used in data fitting. Three datasets were fitted separately.

780 *Model fitting for trial-by-trial adaptation and proprioception changes*. The trial-by-trial
781 changes of adaptation (Figure 3A) and of proprioceptive localization (Figure 4A) was fitted
782 with Eq. 1, Eq. 2, and Eq. 4 based on the mean performance of all participants. The PEA
783 model only had four free parameters, $\Theta = [\sigma_u, \sigma_p, A, B]$. The slope *a* and intercept *b* in Eq.
784 1 were obtained by psychometric tests from Experiment 1 (see statistical analysis). The
785 reported hand position (x_{report}, blue dots in Figure 4A) was based on the proprioceptive
786 cue x_p and the estimated hand $\hat{x}_{Hand}$ from the reaching trial. With the Bayesian cue
787 combination assumption, the reported hand position was biased by x_p with a ratio
788 determined by the variance of x_p and $\hat{x}_{Hand}$:

789 $$x_{report} = \hat{x}_{Hand} + \frac{\sigma_{Hand}^2}{\sigma_{Hand}^2 + \sigma_p^2}(x_p - \hat{x}_{Hand}), \quad (8)$$

790 where σ_{Hand}^2 and σ_p^2 are the variance of $\hat{x}_{Hand}$ and x_p respectively. To verify if the slope *b*
791 and intercept *a* obtained from Experiment 1 are consistent across experiments, they were
792 also estimated by fitting data from Experiment 2 (Figure 3). In this case, the model fitting
793 was performed with 6 free parameters, $\Theta = [\sigma_u, \sigma_p, a, b, A, B]$. The fitted values of *a* and *b*
794 are fallen into the 95% CI of estimated parameters in Experiment 1 (purple line in Figure
795 2C, see details in Table S1).

796 The dependence of proprioceptive recalibration on perturbation size (Figure 4B) were
797 simulated by the PEA model with the parameter values estimated from Experiment 2. We
798 assumed that the proprioceptive bias results from the influence of a biased hand estimate
799 ($\hat{x}_{Hand}$) during adaptation and the influence is quantified as a percentage of its deviation
800 from the true hand location:

801 $$x_{bias} = -(0 - \hat{x}_{Hand})R_p, \quad (9)$$

where the actual hand location is 0, R_p is the percentage of influence, and $\hat{x}_{Hand}$ is determined by Eq.1. In simulation, R_p varied from 0.05 to 0.8 to estimate the overall dependence of proprioceptive recalibration on perturbation size.

Model fitting and simulation for single-trial learning. In the single-trial learning paradigm (Figure S5), the average movement direction across trials aligns with the target direction since the visual perturbations are evenly distributed in both directions. Thus, the sensory cue x_u and x_p have the same mean. For modeling single-trial learning, instead of having two separate cues, we assume a combined cue of x_u and x_p to follow $x_{int} \sim N(T, \sigma_{int}^2)$, where T is the target direction, $\sigma_{int}^2 = \frac{\sigma_u^2 \sigma_p^2}{\sigma_u^2 + \sigma_p^2}$ represents the variance of integrated sensory signal of x_u and x_p. Single-trial learning was quantified as the difference between the two null trials before and after the perturbation trial. As the perturbation size in the triplet of trials varied randomly, we assume that the effects of different perturbations are independent. Thus, single-trial learning was modeled as learning from the current perturbation without history effect. It follows the equations modified from Eq. 1 and 2:

$$x_{STL} = B(T - \hat{x}_{Hand}) \tag{10}$$

$$\hat{x}_{Hand} = W_{int} T + W_v x_v, \text{ with } W_{int} = \frac{1/\sigma_{int}^2}{\sum_j 1/\sigma_j^2},\ i, j = int, v, \tag{11}$$

where x_v is the visual perturbation, W_{int} and W_v are the weights of the cues, σ_v is the standard deviation of the visual cue specified by Eq.4. Parameter set $\Theta = [\sigma_{int}, a, b, B]$ was fitted to the average data from all participants. Model simulations (Figure 5A) were performed with the same single-trial learning equations. For the clear cursor condition, we used the same parameter values estimated from Experiment 2 (see details in Table

S1). For the blurred cursor condition, the standard deviation of visual cue was changed to:

$$\sigma_{v,blur} = R_v \sigma_v \tag{12}$$

for the simulation of the increase in visual uncertainty, the ratio R_v varied from 1.1 to 3.

PReMo model

We used the PReMo model to fit the average adaptation extent obtained from Experiment 2 (Figure 3C & Figure S3B). Following the study by (Tsay, Kim, et al., 2022), the hand position at trial *n+1* is:

$$x_{p,n+1} = Ax_{p,n} + B\left(T - x_{per,n}\right), \tag{13}$$

where

$$x_{per,n} = \beta_p + \frac{\sigma_u^2}{\sigma_u^2+\sigma_p^2} x_{p,n}, \tag{14}$$

$$\beta_p = -min\left(\left|\beta_p^{sat}\right|, \left|\eta_p\left(\frac{\sigma_u^2}{\sigma_u^2+\sigma_v^2} x_{v,n} - \frac{\sigma_u^2}{\sigma_u^2+\sigma_p^2} x_{p,n}\right)\right|\right). \tag{15}$$

In data fitting, we used two parameters to represent the ratio between sensory cues: $R_1 = \sigma_u^2/(\sigma_u^2 + \sigma_v^2)$ and $R_2 = \sigma_u^2/(\sigma_u^2 + \sigma_p^2)$. The data were fitted with the parameter set $\Theta = [R_1, R_2, \beta_p^{sat}, \eta_p, A, B]$, where β_p^{sat} is the saturation angle, η_p is a scaling factor, *A* is the retention rate and *B* is the learning rate. For simulating the proprioceptive localization of the hand (Figure 4C), the parameter values estimated from Experiment 2 were used. The bias of hand estimation in the proprioception trials is determined as: $x_{bias} = -(0 - x_{per})R_p$, where ratio R_p varies from 0.05 to 0.8. Thus, similar to the PEA model simulation,

the proprioceptive bias is a fraction of the bias in the hand estimation from the adaptation trials. Single-trial learning (Figure 5B) was simulated with:

$$x_{STL} = B(T - x_{per}), \tag{16}$$

where x_{per} is determined by Eq. 12 and Eq. 13. For the clear condition, we used the parameter values estimated from Experiment 2 with PReMo. For the blurred cursor condition, the standard deviation of visual signal $\sigma_{v,blur}$ increases with a ratio R_v, as in Eq. 12.

Causal inference model

The causal inference model by (Wei & Körding, 2009) was used to fit the data of Experiment 2 (Figure 3D & Figure S3C). The hand position at trial n+1 is updated by learning from visual error at trial n:

$$x_{p,n+1} = Ax_{p,n} + B\big(T - px_{v,n}\big), \tag{17}$$

where *A* and *B* are the retention and learning rates, respectively; *T* is the target direction. Specifically for this model, the learning from error is modulated by the probability (*p*) of causal attribution of visual error to the action or proprioception:

$$p = S\frac{N(x_{v,n},0,\sigma^2)}{N(x_{v,n},0,\sigma^2)+C}, \tag{18}$$

where $x_{v,n}$ is the visual cue at trial n. *S* and *C* are the scaling factors, and σ is the standard deviation of the integrated cue combining visual and proprioceptive cues, following

$$\sigma^2 = \frac{\sigma_v^2\sigma_p^2}{\sigma_v^2+\sigma_p^2} \tag{19}$$

Thus, the data were fitted with five parameters $\Theta = [\sigma, S, C, A, B]$. For simulating single-trial learning with cursor blurring (Figure 5C), the ratio between σ_v and σ_p is fixed as ½. The single-trial leaning was determined as:

$$x_{STL} = B(T - px_v), \tag{20}$$

where *p* is determined by Eq. 18. Put Eq. 12 and Eq. 19 into $\sigma_{blur}^2 = \frac{\sigma_{v,blur}^2 \sigma_p^2}{\sigma_{v,blur}^2 + \sigma_p^2}$, we can calculate the standard deviation of the integrated sensory signal for the blurred cursor: $\sigma_{blur} = \sigma\sqrt{\frac{5R^2}{R^2+4}}$. Simulation was performed with *R* ranging from 1.1 to 3.

Data fitting

All data were fitted using MATLAB (2022b, MathWorks, Natick, MA, US) build-in function *fmincon* with 100 randomly sampled initial values of parameter sets. See Table S1 and Table S2 for the fitted parameter values and comparisons between different models.

Data availability

Data presented in this work are available at:

https://doi.org/10.6084/m9.figshare.24503926.v1.

References

Albert, S. T., Jang, J., Modchalingam, S., Marius't Hart, B., Henriques, D., Lerner, G., Della-Maggiore, V., Haith, A. M., Krakauer, J. W., & Shadmehr, R. (2022). Competition between parallel sensorimotor learning systems. *ELife*, *11*, e65361.

Albert, S. T., Jang, J., Sheahan, H. R., Teunissen, L., Vandevoorde, K., Herzfeld, D. J., & Shadmehr, R. (2021). An implicit memory of errors limits human sensorimotor adaptation. *Nature Human Behaviour*, 1–15.

Avraham, G., Morehead, J. R., Kim, H. E., & Ivry, R. B. (2021). Reexposure to a sensorimotor perturbation produces opposite effects on explicit and implicit learning processes. *PLoS Biology*, *19*(3), e3001147.

Avraham, G., Taylor, J. A., Breska, A., Ivry, R. B., & McDougle, S. D. (2022). Contextual effects in sensorimotor adaptation adhere to associative learning rules. *ELife*, *11*, e75801.

Berniker, M., & Kording, K. (2008). Estimating the sources of motor errors for adaptation and generalization. *Nature Neuroscience*, *11*(12), 1454–1461.

Berniker, M., & Kording, K. (2011). Bayesian approaches to sensory integration for motor control. *Wiley Interdisciplinary Reviews. Cognitive Science*, *2*(4), 419–428.

Bond, K. M., & Taylor, J. A. (2015). Flexible explicit but rigid implicit learning in a visuomotor adaptation task. *Journal of Neurophysiology*, *113*(10), 3836–3849.

Burge, J., Ernst, M. O., & Banks, M. S. (2008). The statistical determinants of adaptation rate in human reaching. *Journal of Vision*, *8*(4), 1–19.

897 Cheng, S., & Sabes, P. N. (2006). Modeling sensorimotor learning with linear dynamical
898 systems. *Neural Computation*, *18*(4), 760–793.

899 Cressman, E. K., & Henriques, D. Y. P. (2009). Sensory recalibration of hand position
900 following visuomotor adaptation. *Journal of Neurophysiology*, *102*(6), 3505–3518.

901 Della-Maggiore, V., & McIntosh, A. R. (2005). Time course of changes in brain activity
902 and functional connectivity associated with long-term adaptation to a rotational
903 transformation. *Journal of Neurophysiology*, *93*(4), 2254–2262.

904 Donchin, O., Francis, J. T., & Shadmehr, R. (2003). Quantifying generalization from trial-
905 by-trial behavior of adaptive systems that learn with basis functions: theory and
906 experiments in human motor control. *The Journal of Neuroscience: The Official*
907 *Journal of the Society for Neuroscience*, *23*(27), 9032–9045.

908 He, K., Liang, Y., Abdollahi, F., Bittmann, M. F., Körding, K., & Wei, K. (2016). The
909 statistical determinants of the speed of motor learning. *PLoS Computational*
910 *Biology*, *12*(9), e1005023.

911 Henriques, D. Y. P., & Cressman, E. K. (2012). Visuomotor adaptation and proprioceptive
912 recalibration. *Journal of Motor Behavior*, *44*(6), 435–444.

913 Herzfeld, D. J., Vaswani, P. A., Marko, M. K., & Shadmehr, R. (2014). A memory of errors
914 in sensorimotor learning. *Science*, *345*(6202), 1349–1353.

915 Huberdeau, D. M., Krakauer, J. W., & Haith, A. M. (2019). Practice induces a qualitative
916 change in the memory representation for visuomotor learning. *Journal of*
917 *Neurophysiology*, *122*(3), 1050–1059.

Hutter, S. A., & Taylor, J. A. (2018). Relative sensitivity of explicit reaiming and implicit motor adaptation. *Journal of Neurophysiology*, *120*(5), 2640–2648.

Izawa, J., & Shadmehr, R. (2011). Learning from sensory and reward prediction errors during motor adaptation. *PLoS Computational Biology*, *7*(3), e1002012.

Kim, H. E., Morehead, J. R., Parvin, D. E., Moazzezi, R., & Ivry, R. B. (2018). Invariant errors reveal limitations in motor correction rather than constraints on error sensitivity. *Communications Biology*, *1*(1), 19.

Kirk, R. (1968). *Experimental design: Procedures for the behavioral sciences* (Vol. 1–f). Brooks/Cole.

Klein, S. A., & Levi, D. M. (1987). Position sense of the peripheral retina. *JOSA A*, *4*(8), 1543–1553.

Körding, K., & Wolpert, D. M. (2004). Bayesian integration in sensorimotor learning. *Nature*, *427*(6971), 244–247.

Krakauer, J. W., Ghez, C., & Ghilardi, M. F. (2005). Adaptation to visuomotor transformations: consolidation, interference, and forgetting. *The Journal of Neuroscience: The Official Journal of the Society for Neuroscience*, *25*(2), 473–478.

Krakauer, J. W., Hadjiosif, A. M., Xu, J., Wong, A. L., & Haith, A. M. (2019). Motor learning. *Comprehensive Physiology*, *9*(2), 613–663.

Landi, S. M., Baguear, F., & Della-Maggiore, V. (2011). One week of motor adaptation induces structural changes in primary motor cortex that predict long-term memory

939 one year later. *The Journal of Neuroscience: The Official Journal of the Society for*
940 *Neuroscience*, *31*(33), 11808–11813.

941 Leow, L.-A., Marinovic, W., de Rugy, A., & Carroll, T. J. (2020). Task errors drive
942 memories that improve sensorimotor adaptation. *Journal of Neuroscience*, *40*(15),
943 3075–3088.

944 Levi, D. M., Klein, S. A., & Yap, Y. L. (1987). Positional uncertainty in peripheral and
945 amblyopic vision. *Vision Research*, *27*(4), 581–597.

946 Lieberman, H. R., & Pentland, A. P. (1982). Microcomputer-based estimation of
947 psychophysical thresholds: the best PEST. *Behavior Research Methods &*
948 *Instrumentation*, *14*(1), 21–25.

949 Mazzoni, P., & Krakauer, J. W. (2006). An implicit plan overrides an explicit strategy
950 during visuomotor adaptation. *The Journal of Neuroscience: The Official Journal*
951 *of the Society for Neuroscience*, *26*(14), 3642–3645.

952 McDougle, S. D., Bond, K. M., & Taylor, J. A. (2015). Explicit and Implicit Processes
953 Constitute the Fast and Slow Processes of Sensorimotor Learning. *The Journal of*
954 *Neuroscience: The Official Journal of the Society for Neuroscience*, *35*(26).

955 Mikulasch, F. A., Rudelt, L., & Priesemann, V. (2022). Visuomotor mismatch responses
956 as a hallmark of explaining away in causal inference. *Neural Computation*, *35*(1),
957 27–37.

958 Miyamoto, Y. R., Wang, S., & Smith, M. A. (2020). Implicit adaptation compensates for
959 erratic explicit strategy in human motor learning. *Nature Neuroscience*, *23*(3), 443–
960 455.

961 Modchalingam, S., Vachon, C. M., 't Hart, B. M., & Henriques, D. Y. P. (2019). The effects
962 of awareness of the perturbation during motor adaptation on hand localization.
963 *PloS One*, *14*(8), e0220884.

964 Morehead, J. R., Taylor, J. A., Parvin, D. E., & Ivry, R. B. (2017). Characteristics of implicit
965 sensorimotor adaptation revealed by task-irrelevant clamped feedback. *Journal of*
966 *Cognitive Neuroscience*, *29*(6), 1061–1074.

967 Mostafa, A. A., 't Hart, B. M., & Henriques, D. Y. P. (2019). Motor learning without moving:
968 proprioceptive and predictive hand localization after passive visuoproprioceptive
969 discrepancy training. *PloS One*, *14*(8), e0221861.

970 Neville, K. M., & Cressman, E. K. (2018). The influence of awareness on explicit and
971 implicit contributions to visuomotor adaptation over time. *Experimental Brain*
972 *Research. Experimentelle Hirnforschung. Experimentation Cerebrale*, *236*(7),
973 2047–2059.

974 Oh, Y., & Schweighofer, N. (2019). Minimizing Precision-Weighted Sensory Prediction
975 Errors via Memory Formation and Switching in Motor Adaptation. *The Journal of*
976 *Neuroscience: The Official Journal of the Society for Neuroscience*, *39*(46), 9237–
977 9250.

978 Oldfield, R. C. (1971). The assessment and analysis of handedness: the Edinburgh
979 inventory. *Neuropsychologia*, *9*(1), 97–113.

980 Rossi, C., Bastian, A. J., & Therrien, A. S. (2021). Mechanisms of proprioceptive
981 realignment in human motor learning. *Current Opinion in Physiology*, *20*, 186–197.

982 Ruttle, J. E., Cressman, E. K., 't Hart, B. M., & Henriques, D. Y. P. (2016). Time course
983 of reach adaptation and proprioceptive recalibration during visuomotor learning.
984 *PloS One*, *11*(10), e0163695.

985 Ruttle, J. E., 't Hart, B. M., & Henriques, D. Y. P. (2018). The fast contribution of visual-
986 proprioceptive discrepancy to reach aftereffects and proprioceptive recalibration.
987 *PloS One*, *13*(7), e0200621.

988 Ruttle, J. E., 't Hart, B. M., & Henriques, D. Y. P. (2021). Implicit motor learning within
989 three trials. *Scientific Reports*, *11*(1), 1627.

990 Salomonczyk, D., Cressman, E. K., & Henriques, D. Y. P. (2011). Proprioceptive
991 recalibration following prolonged training and increasing distortions in visuomotor
992 adaptation. *Neuropsychologia*, *49*(11), 3053–3062.

993 Salomonczyk, D., Cressman, E. K., & Henriques, D. Y. P. (2013). The role of the cross-
994 sensory error signal in visuomotor adaptation. *Experimental Brain Research.*
995 *Experimentelle Hirnforschung. Experimentation Cerebrale*, *228*(3), 313–325.

996 Seilheimer, R. L., Rosenberg, A., & Angelaki, D. E. (2014). Models and processes of
997 multisensory cue combination. *Current Opinion in Neurobiology*, *25*, 38–46.

998 Shadmehr, R., Smith, M. A., & Krakauer, J. W. (2010). Error correction, sensory prediction,
999 and adaptation in motor control. *Annual Review of Neuroscience*, *33*, 89–108.

1000 Simani, M. C., McGuire, L. M. M., & Sabes, P. N. (2007). Visual-shift adaptation is
1001 composed of separable sensory and task-dependent effects. *Journal of*
1002 *Neurophysiology*, *98*(5), 2827–2841.

1003 Smith, M. A., Ghazizadeh, A., & Shadmehr, R. (2006). Interacting adaptive processes
1004 with different timescales underlie short-term motor learning. *PLoS Biology*, *4*(6),
1005 e179.

1006 Stetson, C., Cui, X., Montague, P. R., & Eagleman, D. M. (2006). Motor-sensory
1007 recalibration leads to an illusory reversal of action and sensation. *Neuron*, *51*(5),
1008 651–659.

1009 ‘t Hart, B. M., & Henriques, D. Y. P. (2016). Separating predicted and perceived sensory
1010 consequences of motor learning. *PloS One*, *11*(9), e0163556.

1011 Taylor, J. A., & Ivry, R. B. (2011). Flexible cognitive strategies during motor learning.
1012 *PLoS Computational Biology*, *7*(3), e1001096.

1013 Taylor, J. A., Krakauer, J. W., & Ivry, R. B. (2014). Explicit and implicit contributions to
1014 learning in a sensorimotor adaptation task. *The Journal of Neuroscience: The*
1015 *Official Journal of the Society for Neuroscience*, *34*(8), 3023–3032.

1016 Thoroughman, K. A., & Shadmehr, R. (2000). Learning of action through adaptive
1017 combination of motor primitives. *Nature*, *407*(6805), 742.

1018 Tsay, J. S., Avraham, G., Kim, H. E., Parvin, D. E., Wang, Z., & Ivry, R. B. (2021). The
1019 effect of visual uncertainty on implicit motor adaptation. *Journal of*
1020 *Neurophysiology*, *125*(1), 12–22.

1021 Tsay, J. S., Haith, A. M., Ivry, R. B., & Kim, H. E. (2022). Interactions between sensory
1022 prediction error and task error during implicit motor learning. *PLoS Computational*
1023 *Biology*, *18*(3), e1010005.

1024 Tsay, J. S., Kim, H. E., Parvin, D. E., Stover, A. R., & Ivry, R. B. (2021). Individual
1025 differences in proprioception predict the extent of implicit sensorimotor adaptation.
1026 *Journal of Neurophysiology*, *125*(4), 1307–1321.

1027 Tsay, J. S., Kim, H., Haith, A. M., & Ivry, R. B. (2022). Understanding implicit sensorimotor
1028 adaptation as a process of proprioceptive re-alignment. *ELife*, *11*, e76639.

1029 Tsay, J. S., Parvin, D. E., & Ivry, R. B. (2020). Continuous reports of sensed hand position
1030 during sensorimotor adaptation. *Journal of Neurophysiology*, *124*(4), 1122–1130.

1031 Tseng, Y., Diedrichsen, J., Krakauer, J. W., Shadmehr, R., & Bastian, A. J. (2007).
1032 Sensory prediction errors drive cerebellum-dependent adaptation of reaching.
1033 *Journal of Neurophysiology*, *98*(1), 54.

1034 Wei, K., & Körding, K. (2009). Relevance of error: what drives motor adaptation? *Journal*
1035 *of Neurophysiology*, *101*(2), 655–664.

1036 Wei, K., & Körding, K. (2010). Uncertainty of feedback and state estimation determines
1037 the speed of motor adaptation. *Frontiers in Computational Neuroscience*, *4*, 11.

1038 Wolpert, D. M., Diedrichsen, J., & Flanagan, J. R. (2011). Principles of sensorimotor
1039 learning. *Nature Reviews. Neuroscience*, *12*(12), 739.

1040 Wozny, D. R., & Shams, L. (2011). Recalibration of auditory space following milliseconds
1041 of cross-modal discrepancy. *Journal of Neuroscience*, *31*(12), 4607–4612.

1042 Wu, H. G., Miyamoto, Y. R., Castro, L. N. G., Ölveczky, B. P., & Smith, M. A. (2014).
1043 Temporal structure of motor variability is dynamically regulated and predicts motor
1044 learning ability. *Nature Neuroscience*, *17*(2), 312.

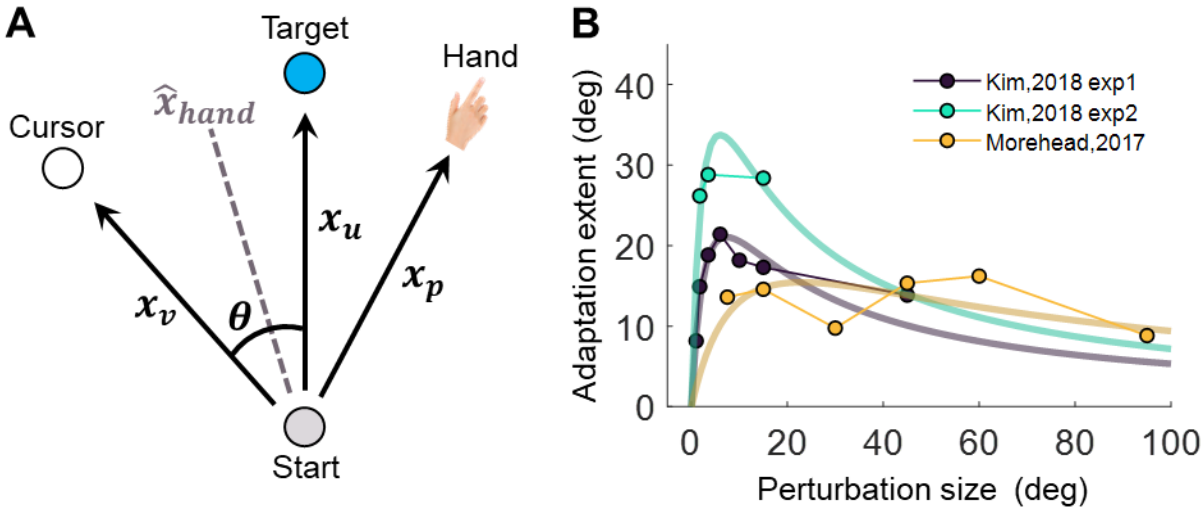

Figure 1. The Perceptual Error Adaptation (PEA) model for error-clamp adaptation. **(A)** Illustration of involved sensorimotor cues for estimating hand direction $\hat{x}_{Hand}$. The clamped cursor, the hand, and the sensory prediction of the reaching action provide the visual (x_v), proprioceptive (x_p), and the sensory prediction cue (x_u) of movement direction, respectively. The hand direction estimate is assumed to be based on maximum likelihood cue combination. **(B)** Assuming a linear dependency of visual uncertainty on eccentricity, the PEA model predicts that implicit adaptation extent is a concave function of perturbation size θ, a pattern qualitatively aligning with previous findings (Kim et al., 2018; Morehead et al., 2017).

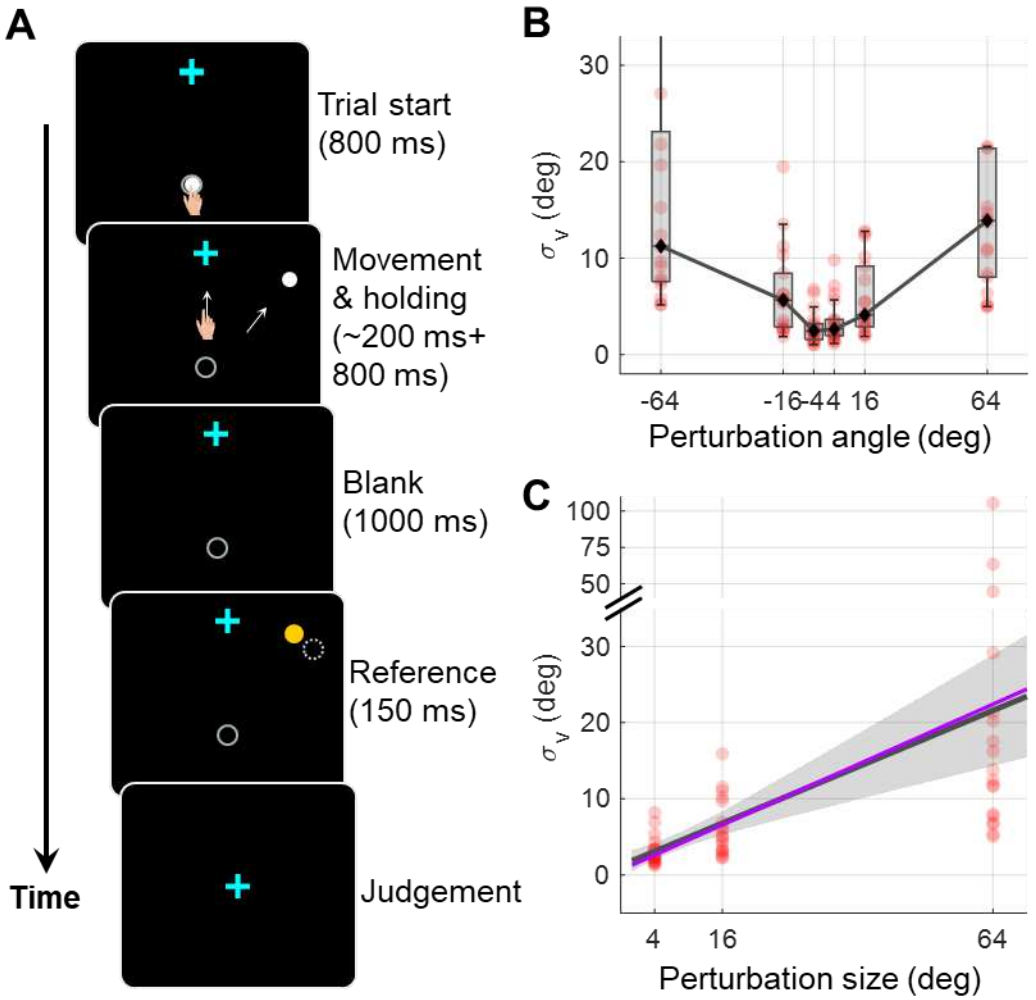

Figure 2. Experiment 1 measuring the dependency of visual uncertainty on perturbation size. **(A)** The 2AFC task for judging the cursor motion direction. In an exemplary trial, the participant reaches to a target while a direction-clamped cursor moves concurrently, serving as an error-clamp perturbation. Following a 1000-ms blank masking period, a reference point appears for 150ms, either clockwise or counterclockwise from the clamped cursor. The participant is then asked to making a binary judgement regarding the direction of the clamped cursor relative to the reference point. **(B)** The visual uncertainty, obtained from psychometrical estimation based on the 2AFC, is plotted as a function of perturbation size. Both individual estimates (red dots) and group-level statistics

(boxplots) are shown. Positive angles correspond to CW rotations, negative angles to CCW rotations. **(C)** Collapsing data from both rotation directions, we observe that visual uncertainty closely follows a linear function of perturbation size. The dark gray line and its shaded region denote the regression line and its 95% confidence interval, respectively. The purple line is generated with the values of *a* and *b* fitted from data in Experiment 2 with *a* and *b* treated as free parameters (See Methods for details).

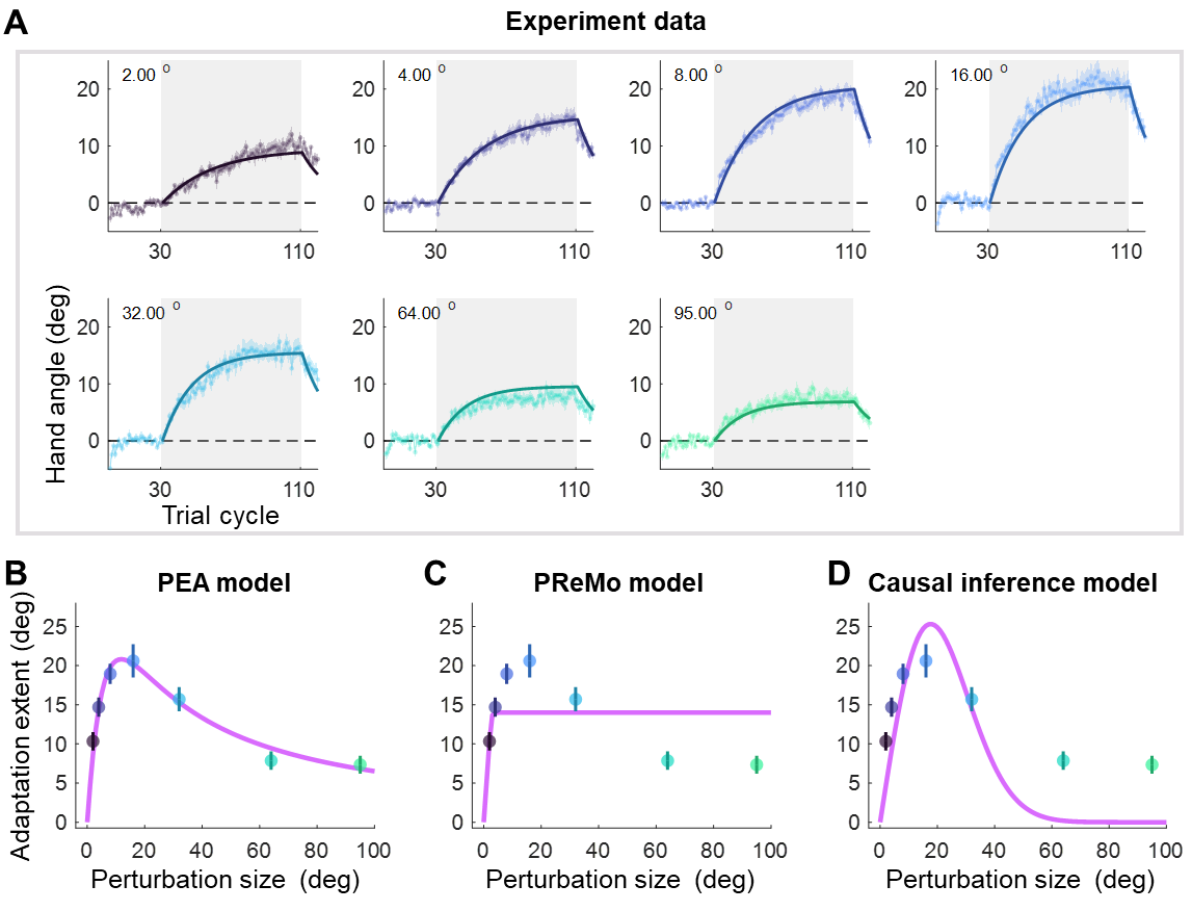

Figure 3. Results and model fitting of Experiment 2. **(A)** Implicit adaptation to error clamps of varying sizes is depicted; colored dot-lines and colored shading area represent the mean and standard error for each participant group. The light gray area indicates trials with error-clamp perturbations. Adaptation starts after baseline, gradually asymptotes to its final extent, and then decays with null feedback during washout. Different perturbation sizes result in distinct adaptation rates and extents. Group averages and standard error across participants are shown, along with predictions (colored solid lines) from the PEA model. **(B)** The adaptation extent (cycle 100-110) exhibits a nonlinear dependency on perturbation size, conforming to a concave function as prescribed by PEA (purple line). Color dots and error bars denote the mean and standard error across participants in each

group. **(C)-(D)** The same data fitted with the PReMo model and the causal inference model. See more details, refer to Figure S3.

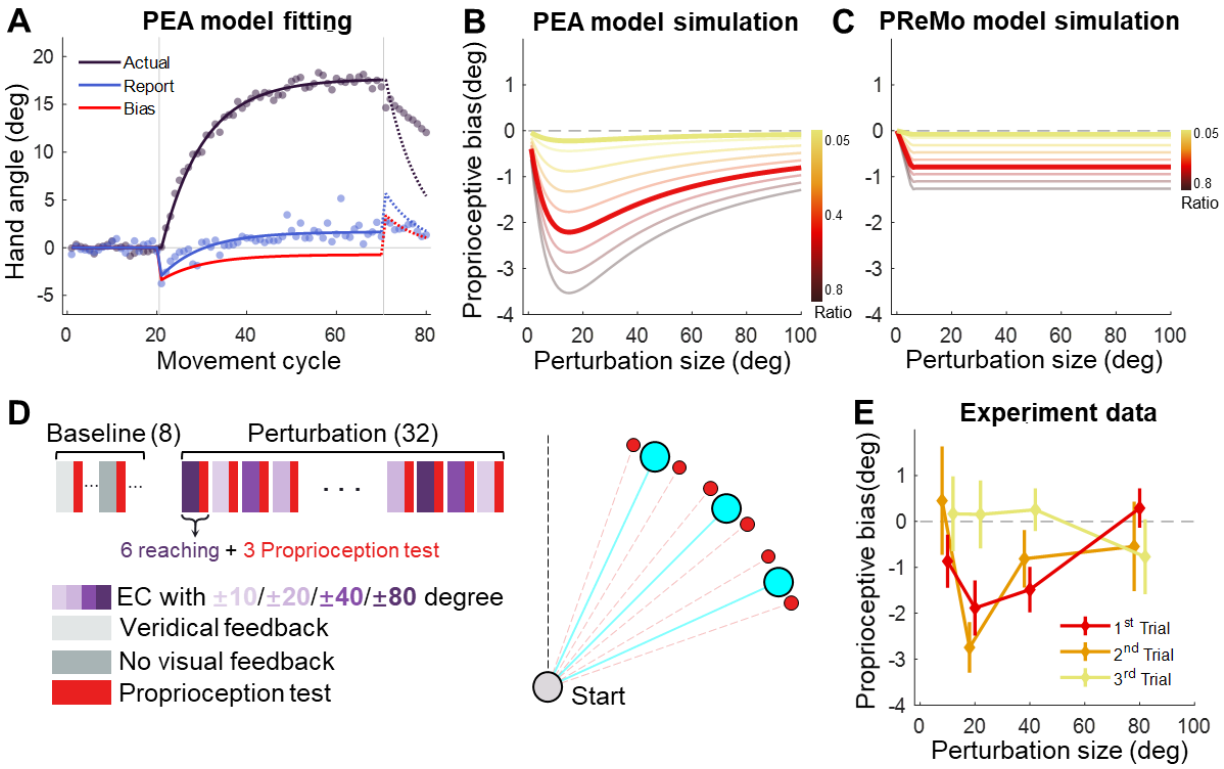

Figure 4. Proprioceptive data fitting and results from Experiment 3. **(A)** The data from (Tsay et al., 2020) are presented alongside the fitting of the PEA model. Participants adapting to a 30° error-clamp perturbation were required to report the location of their adapted hand using visual aids of numbers. The report was provided when the hand stayed at the end of movement. Initially, the proprioceptive estimate of the hand is biased toward the visual cursor (negative in the plot) and then gradually shifts toward the hand (positive in the plot). This trend is accurately captured by the PEA model: lines represent model fitting results, with the adapted hand direction in indigo and the reported hand direction in blue. The hand direction estimate ($\hat{x}_{Hand}$, Eq.1) following a reach movement is shown in red. **(B)-(C)** Model simulations for proprioceptive bias from the PEA and PReMo models. Color gradients denote the simulations with varying ratio between the weights of $\hat{x}_{Hand}$ and x_p, the two cues available for estimating the hand direction. Note

that the two models prescribe distinct profiles for the dependency of proprioception bias on perturbation size. **(D)** Experimental design. A reaching block, either with or without visual perturbations, is followed by a proprioception test block. The size and direction of the visual perturbation vary across blocks. The proprioception test is conducted when the hand is passively moved to a target (red dots) situated near the reaching target (blue dots). **(E)** The observed proprioceptive bias as a function of perturbation size. Data from the three proprioception test trials are separately plotted. The first trial reveals proprioception biases that form a concave function of perturbation size.

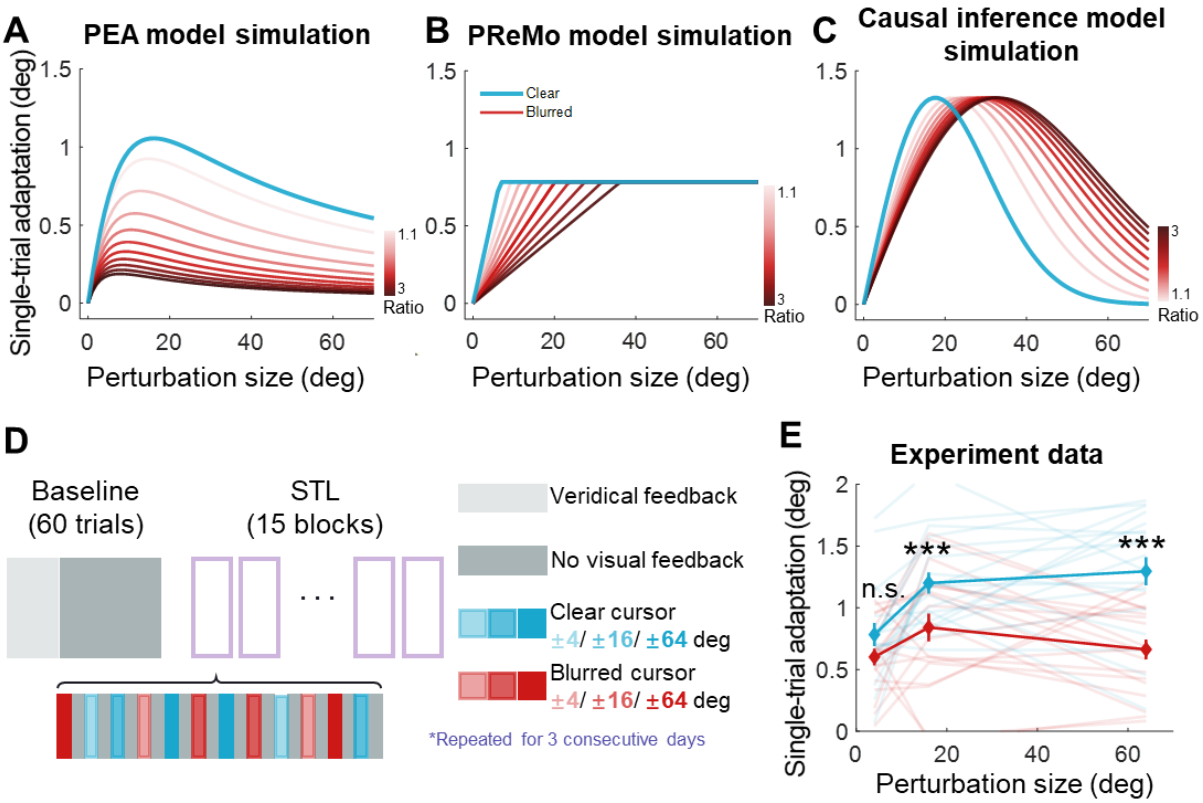

Figure 5. Results of Experiment 4. **(A)-(C)** Model simulations for single-trial learning under different visual uncertainty levels, shown separately for the PEA, PReMo and causal inference models. Blue curves represent simulated learning based on model parameters estimated from Experiment 2. Curves with red gradient indicate simulations with increasing levels of visual uncertainty, color coded by the ratio of visual uncertainty for the blurred cursor to that of the clear cursor. **(D)** Experimental design. Following 60 baseline trials without perturbations, participants completed 15 mini-blocks of error-clamp adaptation over three successive days. Each mini-block features 12 different types of error-clamp perturbations, distinguished by two cursor presentations (blurred or clear cursor) and six clamp sizes. Each perturbation trial, varied randomly in perturbation type, is flanked by two no-feedback trials. The change in hand direction between these two no-

feedback trials serves to quantify singe-trial learning. **(E)** The single-trial learning with the blurred cursor is less than that with the clear cursor, but the difference is non-monotonic across perturbation size (*** denote $p < 0.001$).

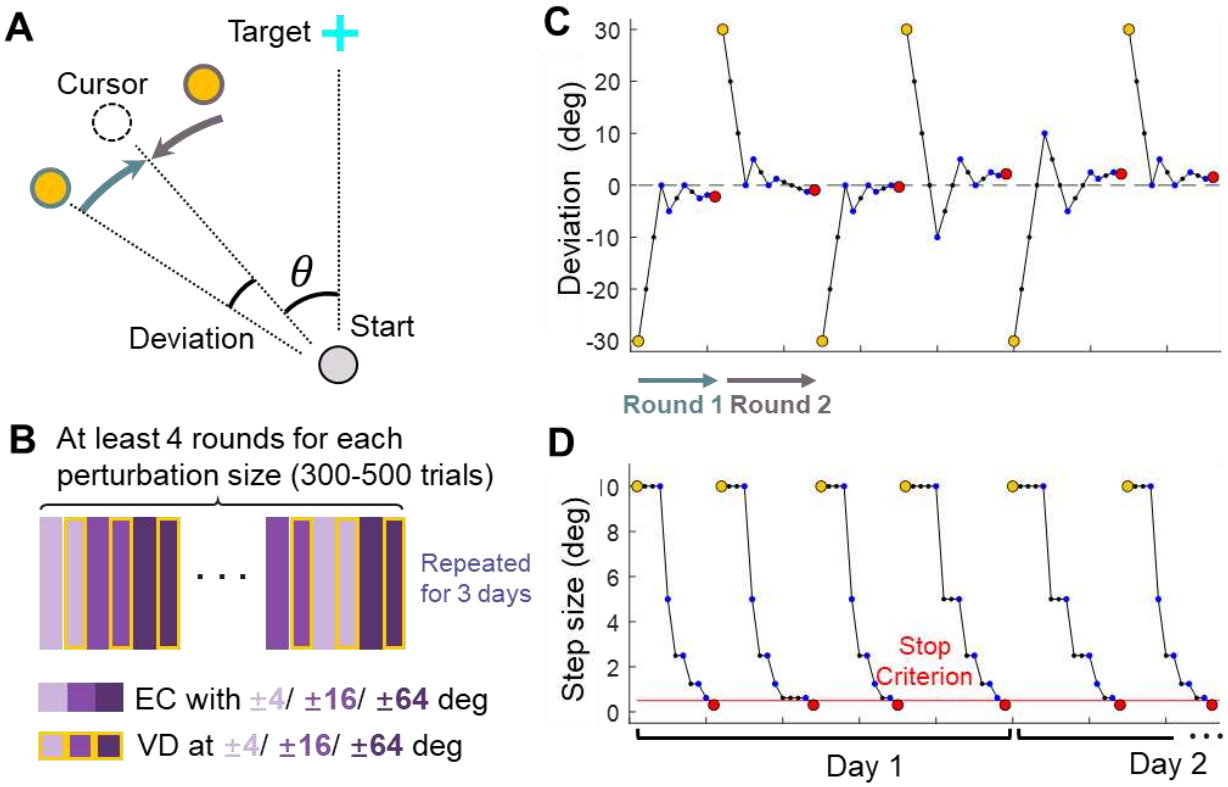

Figure 6. Design of Experiment 1. **(A)** Top-down view of the setup in visual discrimination task. The reference point (yellow) was presented either CW or CCW relative to the clamped cursor (dashed circle), which has a perturbation size θ. **(B)** Trial structure of the visual discrimination task. Purple rectangles represent error-clamped trials with varying perturbation size, rectangles with yellow edges represent the ensuing visual discrimination test for each perturbation size. **(C)-(D)** Exemplary sequences of the reference point: These sequences illustrate the deviation of the reference point from the cursor (C) and the changing step size across trials (D), following the PEST algorithm. Individual trials are represented by blue dots. Yellow and red dots mark the initiation and termination of each round of trials, respectively. In each round, the reference point starts on either the CW or CCW side of the cursor; In the subsequent round, it starts on the opposite side.

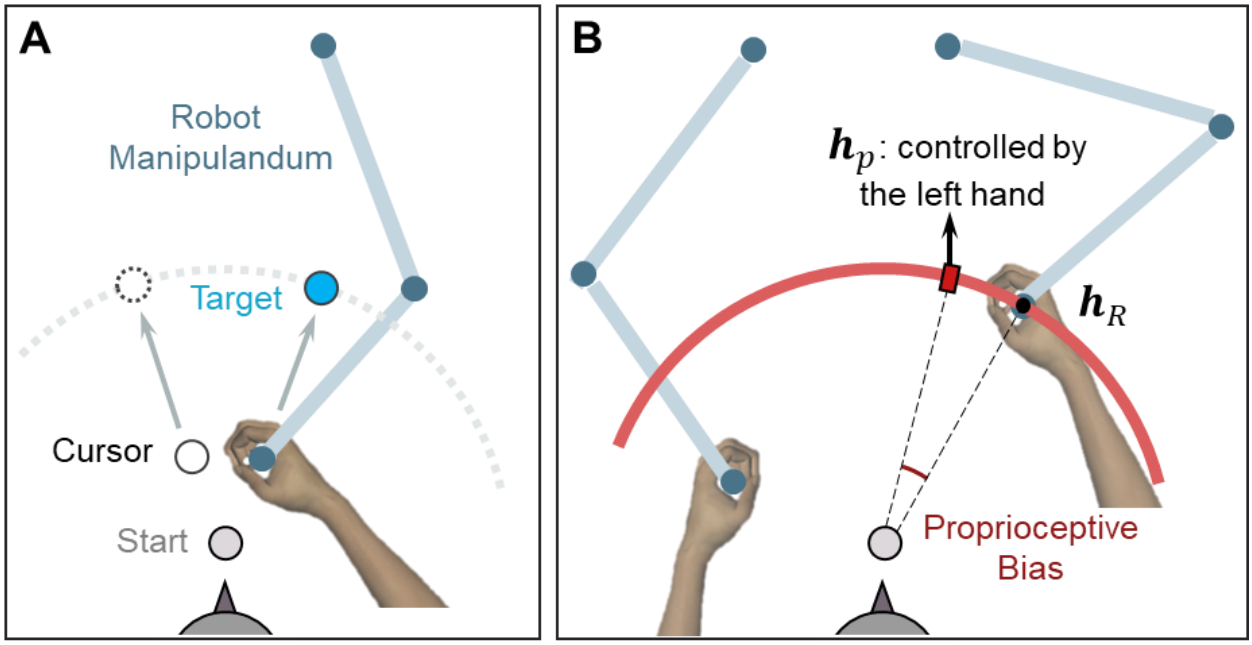

Figure 7. Setup for measuring proprioceptive recalibration in Experiment 3. **(A)** Reaching movement with error-clamped cursor, performed by the right hand holding a robot handle. **(B)** Passive movement in the proprioception test. The right hand was passively moved to the unseen target ($\boldsymbol{h}_R$), depicted here as a small black dot. A red hollow circle with an expanding radius appears on the screen during passive movement, signaling the increasing distance between the hand and the start position. Subsequently, participants used their left hand to report the right-hand location ($\boldsymbol{h}_p$) by aligning a red rectangle on the red circle, which is displayed at the target distance.

Supplementary Materials

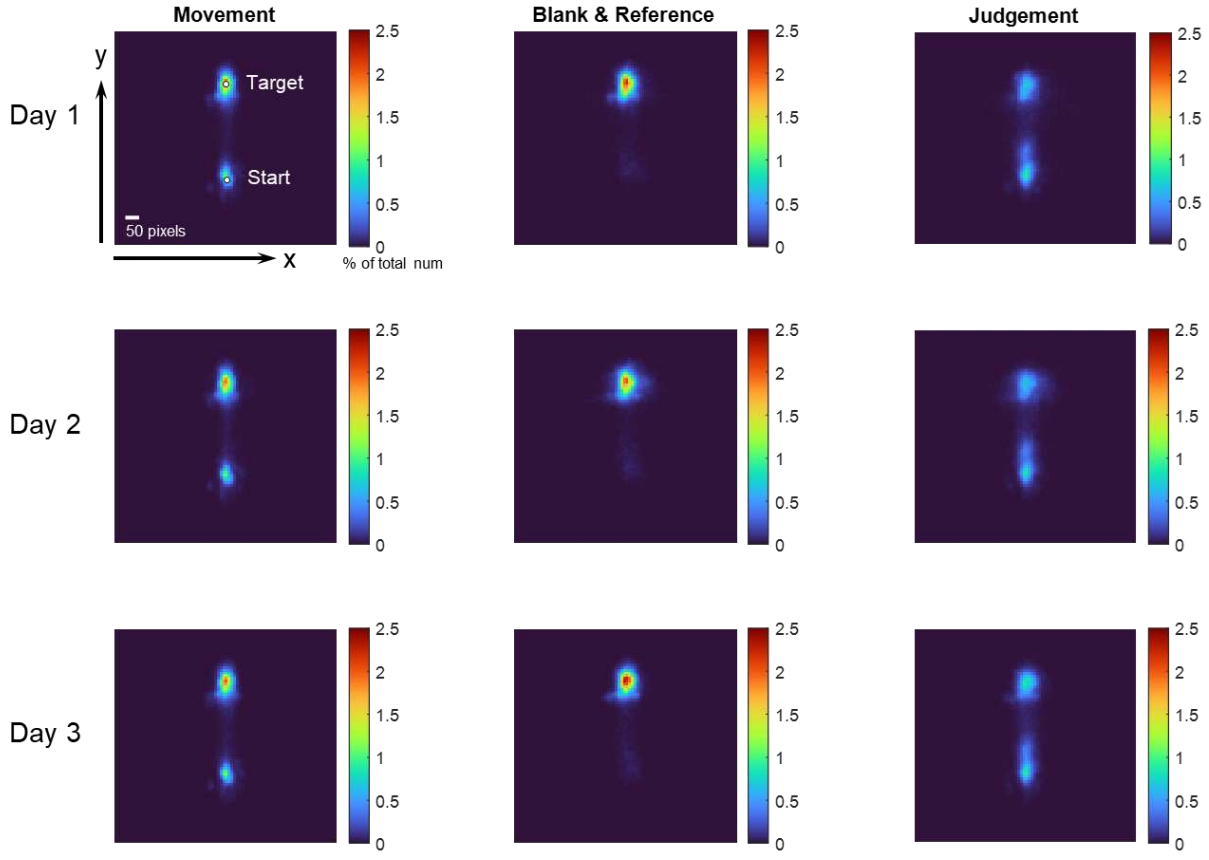

Figure S1. Heat map of eye fixations during the 2AFC task in Experiment 1. The screen is partitioned into 10x10 pixel grids, and the cumulative number of gaze samples in each grid is recorded. Data from all participants, aggregated across each day of practice, are presented. The color map signifies the normalized count of gaze samples in each grid. Data are separately displayed for the three distinct phases of a trial, as delineated by the columns on the left, middle, and right. These correspond to periods during hand movement, the appearance of the visual mask and reference point, and the time allotted for manual response. On average, 95.06%, 89.93%, and 86.55% of gaze samples fall within the ±50-pixel range of the central line during these three phases, respectively.

1155 These results corroborate that participant adhered to the instructions and refrained from

1156 looking at the cursor during the visual discrimination task.

1157

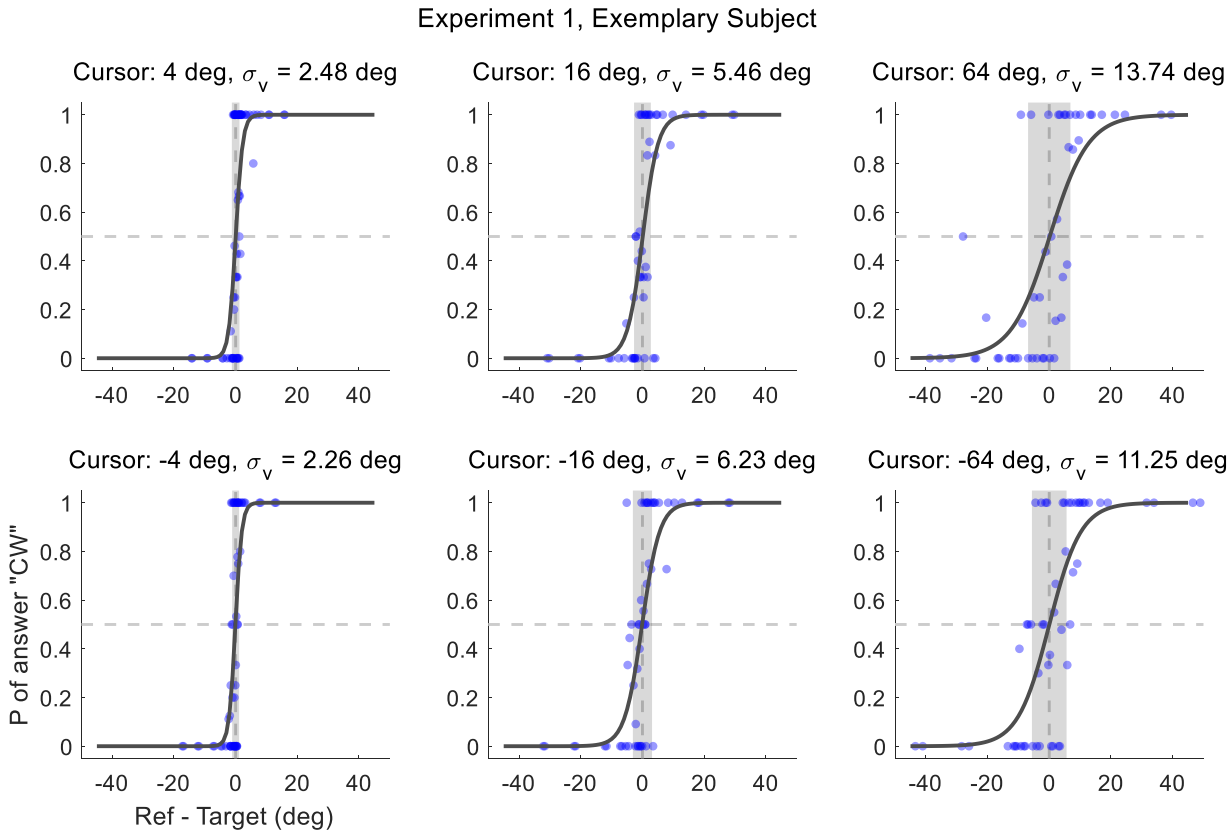

Figure S2. Performance of an exemplary participant in Experiment 1. Six panels display the psychometric curves corresponding to different error-clamp sizes. The x-axis denotes the angular deviation between the clamped cursor and the reference point (as depicted in Figure 6A). A negative value implies that the reference point appears on the counterclockwise (CCW) side of the clamped cursor. The blue dots represent the proportion of trials in which the participant reported that "the yellow point is on the clockwise (CW) side of the clamped cursor" for various angular deviations between these two. Data were aggregated from all trials across three days of the experiment. The gray-shaded region represents the interquartile range (25th to 75th percentile) of the psychometric curve, and the width of this shaded region serves as an indicator of the amplitude of visual uncertainty.

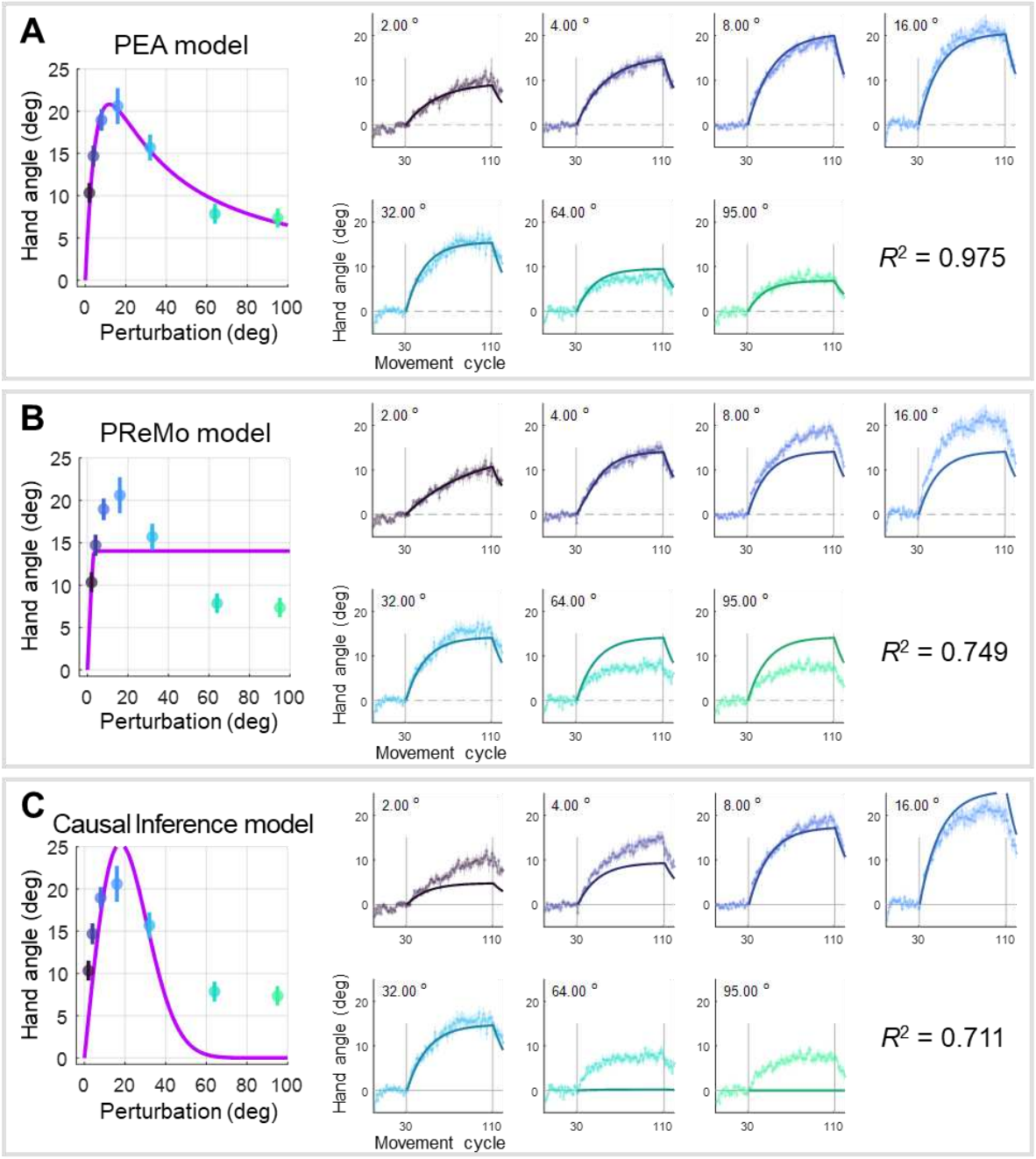

Figure S3. Model fitting for observed implicit adaptation in Experiment 2. This supplementary figure provides a comprehensive evaluation of the three competing models: the PEA model, the PReMo model, and the causal inference model. **(A)** Results of PEA Model Fitting: The layout of these plots mirrors that of Figures 3A and 3B, serving as a direct comparison between the empirical data and the predictions made by the PEA

model. **(B)** Results of PReMo Model Fitting: The left panel is a duplicate of Figure 3C, while the right panel presents the trial-by-trial data fitting. This juxtaposition allows for a nuanced evaluation of the PReMo model's performance at both the aggregate and individual trial levels. **(C)** Results of Causal Inference Model: The arrangement of these plots is consistent with panels (A) and (B), facilitating a straightforward comparison of all three models. For a detailed assessment of the quality of model fitting and subsequent model comparisons, please refer to Table S1 and Table S2.

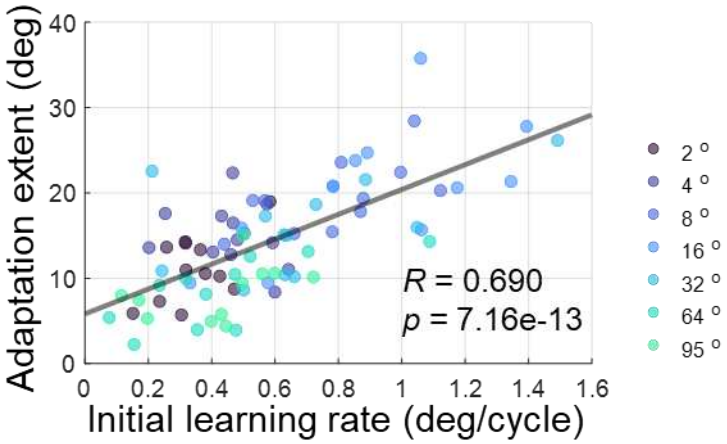

Figure S4. Correlation between initial learning rate and adaptation extent in Experiment 2. For each participant, the initial learning rate is calculated as the change in hand angle between the 1st and 10th cycle, divided by 10. The adaptation extent is defined as the average hand angle across the last 10 adaptation cycles. When pooling data across all perturbation sizes, a significant correlation is observed between the initial learning rate and the adaptation extent.

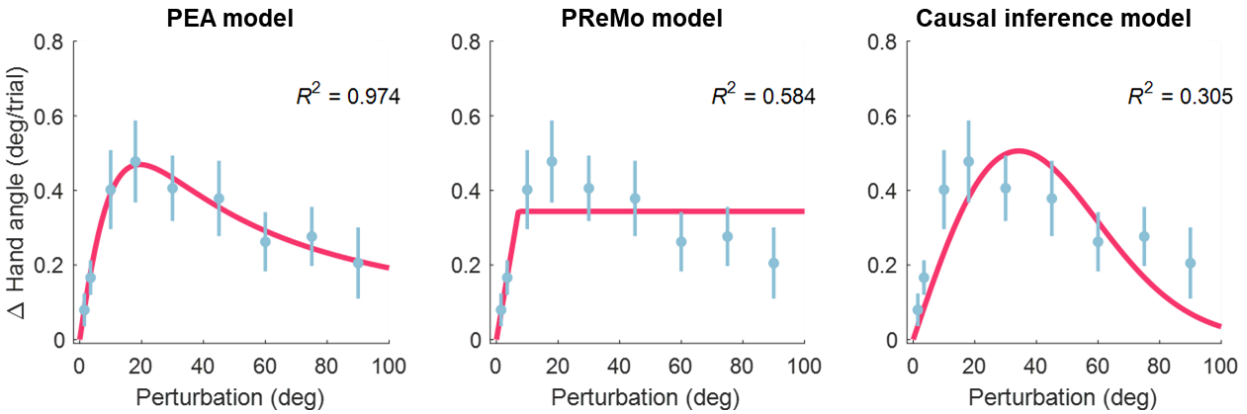

Figure S5. Model fitting of single-trial learning from Experiment 2 of (Tsay, Avraham, et al., 2021). Blue dots represent the mean single-trial learning across varying perturbation size, with error bars represent denoting standard errors across participants. The left, middle and right panel present the fitting results for the PEA, PReMo, and causal inference models, respectively. For additional details, refer to the Methods, Results, and Table S1 & S2.

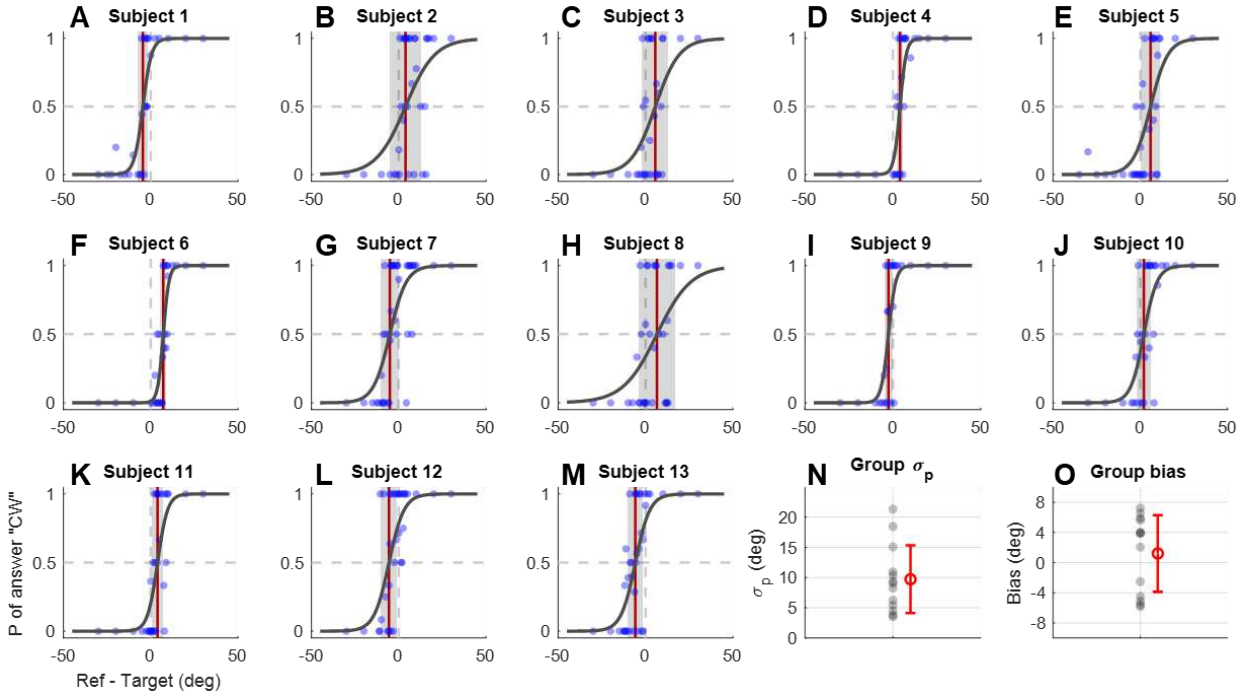

1198

1199 **Figure S6.** Proprioception uncertainty estimation results. Thirteen participants from
1200 Experiment 1 participated in a proprioception discrimination task to measure their
1201 proprioceptive uncertainty in the setting of the error-clamp adaptation. The setup
1202 paralleled that used for estimating visual uncertainty in Experiment 1. In each trial,
1203 participants initially held their hand at the starting position. They were instructed to relax
1204 their arm while the experimenter, seated on the other side of the monitor, pulled their
1205 hand to a proprioceptive target near the straight-ahead target. The arms of the
1206 experimenter and the participant were blocked from the view of the participant. After 0.8
1207 seconds, a yellow reference point appeared. The angular deviation between the
1208 participant's hand and this reference was determined using the same PEST procedure
1209 employed in Experiment 1. Participants indicated, by pressing left or right arrow keys by
1210 their left hand, whether the reference point appeared on the CW or CCW side of their
1211 actual right-hand position. The maximum deviation allowed was 30°, with an initial step

size of 10° and a stop threshold of 0.5°. This task was conducted over six runs across three consecutive days. Similar to Figure S2, panel (A) to (M) show the psychometric curves for each participant with data from the three days pooled together. (N) and (O) present the measured proprioceptive uncertainty and bias for all participants (gray dots) and their mean ± standard deviation (red error bars).

Table S1. Model fitting and simulation parameters with the PEA model.

	Data set	Parameters						Goodness-of-fit	
		σ_u (deg)	σ_p (deg)	*a*	*b*	*A*	*B*	R^2	*RMSE* (deg)
Adaptation extent fitting (Figure 1B)	Kim 2018, Exp1	--	σ_p/a = 3.406; *b*/*a* = 0.138			--	--	0.773	1.898
	Kim 2018, Exp2	--	σ_p/a = 4.758; *b*/*a* = 0.168			--	--	<0	2.163
	Morehead, 2017	--	σ_p/a = 1.639; *b*/*a* = 0.044			--	--	<0	2.937
Trial-by-trial adaptation fitting	Exp 2, Figure 3	5.048	11.119	*1.853	*0.309	0.970	0.208	0.975	1.222
		5.468	12.128	1.663	0.331	0.971	0.194	0.975	1.217
	Tsay 2019, Figure 4A	1.896	7.959	*1.853	*0.309	0.978	0.525	0.991	0.716
Single-trial learning fitting	Tsay 2021, Figure S6	σ_{int} = 7.364		1.179	0.384	--	0.057	0.974	0.020
Proprioceptive recalibration simulation	Exp 3, Figure 4B	5.048	11.119	1.853	0.309	0.970	0.208	--	--
Adaptation affected by visual uncertainty simulation	Exp 4, Figure 5	5.048	11.119	1.853	0.309	--	0.208	--	--

* Asterisks represent fixed parameters in specific data fitting. The fixed values equal to the slope and intercept estimated from Experiment 1.

1221 **Table S2.** Model comparisons.

Data set		*PEA*	*PReMo*	*Causal Inference*
Block-design learning fitting Exp 2, Figure 3 & S3	AIC	2255	3543	3283
	R^2	0.975	0.749	0.711
	$RMSE$ (deg)	1.222	3.896	4.151
Single-trial learning fitting Tsay 2021, Figure S5	AIC	-36.90	-15.98	-11.28
	R^2	0.974	0.584	0.305
	$RMSE$ (deg)	0.020	0.103	0.080

1222